LAWRENCE
LIVERMORE
NATIONAL
LABORATORY

LLNL-JRNL-733037

Species Separation and Other Kinetic Effects at Shock Wave Fronts in Plasma Mixtures Assessed using Molecular Dynamics

K. K. Mackay, W. H. Cabot, T. Haxhimali, J. N. Glosli, H. D. Whitley, R. E. Rudd

June 13, 2017

Physical Review E

Disclaimer

Species Separation and other Kinetic Effects at Shock Wave Fronts in Plasma Mixtures Assessed using Molecular Dynamics

Kyle K. Mackay,* William H. Cabot,† Tomorr Haxhimali,†
James N. Glosli,† Heather D. Whitley,† and Robert E. Rudd‡
Lawrence Livermore National Laboratory, Livermore, CA 94550
University of Illinois at Urbana-Champaign, Urbana, IL 61801
(Dated: September 18, 2017)

The propagation of a shock through a binary plasma mixture of hydrogen isotopes is simulated with molecular dynamics (MD) and a multispecies continuum hydrodynamics model. Separation of the two species due to their mass difference is observed at the shock front in both simulations. We analyze the shock structure in detail to determine which aspects of the wave propagation and shock profile obey single-fluid hydrodynamics and which require multi-component hydrodynamics with Fickian and barodiffusion. In order to reduce possible sources of uncertainty due to transport models used in the continuum simulations, we have performed separate, equilibrium MD simulations which verify the accuracy of the recently proposed Kinetic Molecular Dynamics (KMD) viscosity model, even at the relatively cold pre-shock temperature of 1 eV. We find the post-shock temperature and density are generally consistent between continuum and atomic-scale calculations, but the MD simulations predict a significantly larger thickness of the leading light-ion shock front, with some associated differences in the species separation. We analyze the shape and anisotropy of the MD velocity distributions in detail and compute the electric field at the shock interface from both the MD and continuum simulations. We find that the continuum hydrodynamics calculation captures the major features of the electric field through the electron pressure term in the barodiffusion model and conclude that the differences observed in the shock structures from the two simulations arise largely from non-Maxwellian effects in the longitudinal velocities (the velocities in the direction that the shock propagates) that are not captured in the hydrodynamic simulations.

I. INTRODUCTION

In recent years, several studies have examined how kinetic processes may influence inertial confinement fusion (ICF) experiments [1–8]. Kinetic processes, in this context, are physical phenomena beyond the scope of hydrodynamics in local thermodynamic equilibrium. They are associated with strong gradients, perhaps due to a length scale in the system that is comparable to, or smaller than, the mean free path. They can include everything from ionic transport, such as ion species diffusion at material interfaces [9], to more exotic examples, such as species separation at a shock front[1, 2, 8], the Knudsen processes affecting the tail of the velocity distribution [3, 4, 6], temperature separation between different components in a mixture [2], and anisotropic velocity distributions [7]. They can take place in the presence of hydrodynamic instabilities, and influence the instability growth rate [10]. They encompass phenomena that exhibit non-equilibrium (non-Maxwellian) velocity distributions, including cases due to low collisionality. These phenomena are germane to current efforts in radiation hydrodynamics, such as the `Miranda` code effort [11–13], where multi-component transport models have already been implemented.

Shock waves offer an interesting test case for examining kinetic processes. The shock front thickness provides a short length scale over which the system is driven out of equilibrium. Particle collisions act to restore the system to thermodynamic equilibrium. The classic picture of a shock wave is a step function in density, pressure and other quantities, taking an initial state in thermodynamic equilibrium to a different equilibrium state, known as the Hugoniot state. The final state has additional entropy, and it is particle collisions in the shock front that work to establish the new equilibrium and steady wave propagation. Real shock fronts are not step functions. Dissipative forces arising from the particle collisions act to reduce the gradients near the shock discontinuity and smooth the shock front into the steady wave profile. The shock front is thus broadened by various transport and constitutive properties of the shocked medium: the viscous flow in response to velocity gradients, the thermal conduction in response to temperature gradients, the elasto-plastic response to strain gradients, and the diffusive response to gradients in concentration, pressure and temperature.

For sufficiently weak gradients, these processes can be described by multi-fluid and multi-component hydrodynamic treatments, though many hydrodynamic models applied to study plasmas use the single-fluid assumption.

Species separation in the strong gradients of a shock front is potentially important to ICF due to its impact on isotope ratios in the hot spot during the implosion that can affect fusion [4]. Species separation was first studied analytically by D'yakov[14] and via computer simulations by Sherman, who performed continuum multi-component hydrodynamics simulations of a propagating shock in a binary mixture under the assumption of a common temperature for both species [15].

* University of Illinois at Urbana-Champaign
† Lawrence Livermore National Laboratory
‡ Corresponding author. Electronic address:robert.rudd@llnl.gov; Lawrence Livermore National Laboratory

By "multi-component hydrodynamics," we mean solving the Navier-Stokes equation with a single velocity field allowing for diffusion in the center-of-mass frame. Subsequently, Bird performed Monte Carlo simulations of the Sherman problem and found a temperature spike due to non-Maxwellian velocity distributions within the shock [16]. More recently, particle-in-cell (PIC) simulations and multi-temperature gas models have been used to study shocks in mixtures in more detail [1, 2]. The regime of validity for the PIC simulations is limited to the regime of hot plasmas, where the collision operators derived based on classical plasma physics are valid without the need to account for spatial correlations of the ions.

Recently, molecular dynamics (MD) has emerged as a different approach that can be applied to the study of kinetic effects in shocked plasma[17]. MD simulations provide a capability for studying plasmas from strongly coupled, warm dense conditions to the weakly coupled, hot dilute conditions that are also accessible via PIC. The recent MD simulations studied shock waves in two-dimensional Yukawa systems, quantifying the departure from Maxwellian velocity distributions [17]. The Yukawa or screened Coulomb interaction used in that work provides a good description of the ion dynamics in spatially homogeneous plasmas, including dusty plasma, but modeling shocks in high-energy-density systems have additional requirements. Here we extend the MD simulations of shocked plasma in several significant ways. The first extension is to three dimensions. Making use of the efficient domain decomposition molecular dynamics code `ddcMD` [18] on a supercomputer, it is possible to run large-scale 3D MD simulations of shocks, which is important for realistic collision cross-sections in transport processes. The second extension is to mixtures. Mixtures of two ion species are needed to study species separation at the shock front. The MD simulations handle mixtures naturally, but the associated analysis techniques had to be developed. The third extension is the capability to simulate the change in ionization and screening as the plasma is shock-compressed. For this we make use of the Multiscale Orbital-free DFT Molecular Dynamics (MOD-MD) capability [9] in `ddcMD`, which was developed recently. DFT here means Density Functional Theory. MD simulations of shock waves have not previously included variable ionization or screening to the best of our knowledge. It has been prohibitively expensive to apply the existing variable-electron-density techniques to simulations with the millions of ions needed for shock simulations. The MOD-MD approach provides a multiscale approach to include the spatially varying screening of the electrons without prohibitive cost. Having the correct ionization and screening is important for the plasma equation of state that governs the shock velocity, collision cross-sections that govern tranport, and pressure gradients that drive barodiffusion. The MOD-MD technique also enables calculation of the electric field at the shock front.

We present results for both MD and multi-component hydrodynamic simulations (using `Miranda`) of shock propagation in binary mixtures of ions with atomic number $Z = 1$ and mass ratios ranging from 3 to 20. Carrying out nominally identical simulations with the two approaches enables us to identify phenomena in MD that go beyond the multi-component hydrodynamics of `Miranda`. Indeed, the MD simulations provide data for the verification of other multi-component and multi-fluid models available for use in radiation hydrodynamics codes, as well. In MD, ion transport and the development of the multi-species shock front emerge from the collective behavior of the ions due to the forces between them, avoiding the need for assumptions regarding transport coefficients or collision operators. All kinetic processes that are derived from ion-ion collisions are explicitly present. Specifically, we investigate the influence of the mass ratio on the observed shock profile, the structure of the velocity distributions across the shock front, and the collisional physics of the plasmas are discussed. We generally find that the shock profiles computed using `Miranda` are similar to those computed in `ddcMD`; however, in the MD simulations we find thicker shock fronts associated with the lighter species in the mixture, greater temperature excursions, and significant anisotropic effects in the particle velocity (computed relative to the local fluid velocity) which are not currently included in the multi-component hydrodynamics model in `Miranda`. Our MD results are qualitatively consistent with a previous MD study using hard spheres [19]. We also find good qualitative agreement with the PIC studies [2]. We report new equilibrium MD results for the viscosity of the pre-shocked mixtures and find that they agree well with the Kinetic Molecular Dynamics (KMD) model[20]. A failure of the KMD viscosity model used in `Miranda` could have accounted for the shock profile differences, but the equilibrium MD results demonstrate the accuracy of the model down to the 1 eV temperatures. We discuss similarities and differences between the continuum and MD simulations and conclude that the differences between MD and continuum simulations arise mainly from the non-Maxwellian distributions of ionic velocities ahead of the shock front.

The paper is organized as follows. In Sections II and III, we give a description of the models used for atomic-scale and continuum representation of the binary plasma mixture. Section IV contains a discussion of general shock structure in the binary mixture, including density and temperature profiles across the shock, and separate calculations of ion viscosity at conditions corresponding to ahead of the shock. Section V provides a systematic study of barodiffusion and species separation. Section VI addresses non-Maxwellian behavior and other kinetic effects beyond species diffusion. Finally, we present the conclusions.

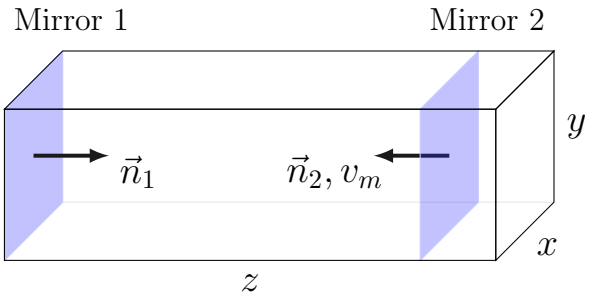

FIG. 1. A schematic of the domain for molecular dynamics shock simulations. The simulation is periodic in the transverse (x and y) directions. The simulation has vacuum beyond the mirrors in the longitudinal (z) direction. Mirror 1 is stationary; mirror 2 moves at the speed $v_m = 80$ nm/ps (80 km/s) in the $-z$ direction, to the left, causing a shock to form and move to the left.

II. MOLECULAR DYNAMICS SIMULATIONS

The MD simulations here have been carried out using the molecular dynamics code `ddcMD` [18], which was developed for efficient massively parallel plasma applications through work of the Cimarron collaboration [21]. MD plasma simulations have already been utilized to study many microphysics problems, including electron-ion equilibration rates [22], charged particle stopping power [23], electron conductivity and thermal conductivity [24, 25], microfields [26, 27], and ionic viscosity and interdiffusion [20, 28, 29]. In this work, we utilize the `ddcMD` capability to study species separation and non-Maxwellian phenomena in shocked plasma mixtures. The conditions studied here are in the moderately strongly to moderately weakly coupled regime, and thus provide a complement to previous work in the hot, dilute regime.

The primary assumption of the MD method applied here is that the Born-Oppenheimer approximation can be applied so that the motion of the electrons is fast compared to that of the motion of the ions. The electrons are thus treated as a neutralizing background that linearly screens the Coulomb charge of the ions. The screening is computed throughout the simulation using an approximate electronic structure method that was recently developed and implemented in `ddcMD` [9]. This technique enables us to run MD simulations on time scales and length scales that are relevant for shocks that account for changes in the electron density, but neglect some electronic effects, such as the electron thermal conduction ahead of the shock front.

The ion interactions are specified by the MOD-MD methodology in `ddcMD` [9]. These interactions are a generalization of the screened Coulomb (Yukawa) interaction [9]. With this potential, electrons are not explicitly simulated, though their effect is included through screening. MOD-MD allows for spatially varying screening lengths, such as those that arise from the differences in the electron density ahead of, and behind, the shock front. The ion charge is calculated on the fly in a Thomas-Fermi solve based on the local ion density and the electron temperature. The electron density is calculated self-consistently between the Fermi integral for thermal occupation and the electric field from a Poisson solve. In addition to the usual spherically symmetric screened Coulomb form, the dipole field of each ion is calculated. A homogeneous electron temperature of 1 eV is assumed throughout the simulated plasma.

The ions move according to Newton's Second Law ($F = ma$), with the set of coupled ordinary differential equations integrated explicitly in time using a velocity Verlet time integrator with a time step of 2×10^{-5} ps.

Periodic boundary conditions are used in the transverse (x and y) directions and momentum mirrors are used to confine the plasma in the longitudinal (z) direction. A schematic of the molecular dynamics simulation domain including mirror placement is shown in Fig. 1.

We have conducted MD simulations of strong shocks in initially equal binary mixtures of hydrogen with another hydrogen isotope 3 to 20 times more massive. MD simulates the motion of particles (atoms, molecules, ions, etc.) interacting by forces derived from an interatomic potential; i.e., a force law that determines the forces on the ions as a function of their positions. Properties of the plasma mixture such as the equation of state, electric fields and transport coefficients emerge naturally from the statistical mechanics of the ions interacting by the specified force law. We use the `ddcMD` particle dynamics code [30], which has been optimized for massively parallel simulations on parallel supercomputers such as the Vulcan BGQ machine used here.

To initialize the system, light and heavy isotopes are positioned in a rock salt configuration to ensure an initially uniform mixture; i.e., the light and heavy isotopes positioned at the corner and center positions, respectively, in a body-centered cubic lattice. The system is brought to thermal equilibrium by increasing the ion temperature to 1 eV over a 0.5 ps interval using a Langevin thermostat. After thermalization of the ions, a shock is driven by a piston consisting of a planar momentum mirror moving down the longitudinal axis. The simulation proceeds until the shock wave reaches the negative z end of the domain, usually on the order of 1-10 ps, depending on the isotopes and system size.

The computational cost of the simulation scales linearly with the number of ions, so the box size is adjusted to be large enough to allow a steady wave to form but no larger. Simulations are repeated with increased box length in the longitudinal direction until temperature profiles and density jump across the shock ceased to change with an increase in box size. In general, plasma mixtures with larger mass ratios require a greater distance for the shock to reach a steady-state condition, and mixtures with the highest mass ratios (H-^{15}H and H-^{20}H) were not able to reach steady-state even with the largest domain sizes tested. The length of the box in the z direction varies between 65 and 340 nm and extends 6.25 nm in both the x and y directions. The transverse

box size is large compared to the mean ion separation and the Debye screening length.

The MD simulations write out many quantities for subsequent analysis, including the local density and velocity distributions for each type of ion. In particular, the simulation box is subdivided into 0.1 nm thick slabs in the longitudinal direction. In each slab, the macroscopic temperature of ions belonging to species α is calculated as

$$\overline{T}_\alpha = \frac{m_\alpha}{3k_B}\left[\left\langle|\mathbf{v}|^2\right\rangle_\alpha - |\langle\mathbf{v}\rangle_\alpha|^2\right], \quad (1)$$

where m_α represents the mass of an ion of type α, angled brackets with the subscript α denote averages only over ions of type α in the slice, and k_B is the Boltzmann constant. The mixture temperature in each slice was calculated as

$$\overline{T}_M = \frac{m}{3k_B}\left[\sum_\alpha^{N_s} y_\alpha \left\langle|\mathbf{v}|^2\right\rangle_\alpha - \left|\sum_\alpha^{N_s} y_\alpha \langle\mathbf{v}\rangle_\alpha\right|^2\right], \quad (2)$$

where $m = \sum_\alpha^{N_s} x_\alpha m_\alpha$ is the mean ion mass, x_α is the mole fraction of species α, $y_\alpha = x_\alpha m_\alpha / m$ is the mass fraction of species α, and N_s is the number of ion species in the system.

These expressions for the temperatures are related to the kinetic energy in the center-of-mass frame, so they are not affected by the overall velocity field (particle velocity) behind the shock.

Directional temperatures are calculated in a similar manner, using only velocity components in the direction of interest. The system may not be in local thermodynamic equilibrium at the shock front. The transverse and longitudinal velocities may be different. As such the quantities T_j and $\overline{T}_M$ are not temperatures in a strict sense. Evaluated in an ensemble average for a system at equilibrium, they give the temperature, and so we will refer to them as temperatures. For the ^{1}H-^{3}H cases presented here, each slab contains approximately 3,900 ions in the pre-shock region and 13,700 in the post-shock region.

A. Momentum Mirrors

Planar momentum mirrors are used to initiate and drive the shock in our molecular dynamics simulations. Each mirror has a centroid position $\vec{r}_m$, and velocity v_m in the direction of its normal vector, $\vec{n}$. If an ion with position $\vec{r}_p$ and velocity $\vec{v}_p$ is found "behind" the mirror (i.e. $(\vec{r}_p - \vec{r}_m)\cdot\vec{n} < 0$) and the ion is moving slower than the mirror in the direction of mirror motion ($\vec{v}_p \cdot \vec{n} < v_m$), the component of ion velocity normal to the mirror ($v_{p,m}$) has its direction flipped in the mirror rest frame according to the transform

$$\begin{aligned} v_{p,m} &= \vec{v}_p \cdot \vec{n} \\ \vec{v}_{p,new} &= \vec{v}_p - 2v_{p,m}\vec{n} + 2v_m\vec{n}. \end{aligned} \quad (3)$$

Ions "in front" of the mirror or moving in the direction of the mirror with $v_{p,m} > v_m$ do not have their velocities modified. In our simulations, mirrors are placed at each extent of the domain in the z-direction with inward-facing normal vectors parallel to the z-axis. The mirror at the lower z end of the domain is assigned a velocity of zero and is used to contain ions in the pre-shock region. The mirror on the positive z end of the domain is assigned a velocity in the -z direction to drive the shock.

B. Strong Collision Scattering Length

Information about each strong collision between ions is collected during MD shock simulations. For these conditions, a "strong collision" is defined as two ions approaching each other within some small cutoff radius r_c. The strong collision scattering length of each ion in the simulation (λ') is calculated as the mean distance it traveled between strong collisions during an interval of length τ = 10 fs. At the end of the interval, the domain is divided into slabs (identical to the slabs used for temperature calculations) and statistics were collected on the scattering length of ions within each slab. In particular, we calculate the slab-wise average scattering length,

$$\langle\lambda'\rangle = \frac{1}{N_i}\sum_j^{N_i}\lambda'_j, \quad (4)$$

standard deviation of scattering length,

$$\sigma_\lambda = \sqrt{\frac{1}{N_i}\sum_j^{N_i}(\lambda'_j - \langle\lambda'\rangle)^2}, \quad (5)$$

and collision frequency,

$$\omega_c = \frac{1}{\tau N_i}\sum_j^{N_i} N_{c,j}, \quad (6)$$

where N_i is the number of ions in the slab, $N_{c,j}$ is the number of collisions experienced by ion j, and λ'_j is the scattering length of ion j over the simulated time interval τ.

C. Computational Cost

A typical run used 512-1024 nodes of 16 cores each and 2 threads per core on the Vulcan BGQ supercomputer [31]. A shock simulation required 20-40 hours of wallclock time to run to completion. An evolving orthorhombic spatial domain decomposition was used to achieve computational load balance between the compressed and uncompressed regions to improve the performance [32]. Optimized parallel I/O for checkpoints and analysis files further improved the performance.

III. CONTINUUM MODEL

Shock propagation has been studied extensively in the context of continuum hydrodynamics [33, 34]. It is well known that analyzing the conservation equations for mass, momentum and energy in the frame of a steady shock leads to the Rankine-Hugoniot jump conditions [33]. Application of the steady wave conditions through the shock profile leads to the Rayleigh line description of the states in the shock front. Here we apply this approach to the case of a binary plasma mixture including species diffusion fluxes with contributions from Fickian (concentration gradient-driven) diffusion, barodiffusion and thermodiffusion. Both ion and electron contributions to barodiffusion and thermodiffusion are included. The jump conditions give analytic relations between the thermodynamic states well in front of, and well behind, the shock. The code `Miranda` is used to calculate quantities like the shock profile for which no analytic expression is available.

A. Governing Equations

The continuum hydrodynamics code `Miranda` uses a single mass-weighted velocity, single ion temperature, and a standard Chapman-Enskog model to describe the transport of ion species. As such, it is a multi-component hydrodynamics code that accounts for kinetic effects at the level of linear-response species diffusivity, viscosity and thermal conductivity. The continuum code uses high-order spatial differencing and time discretization as described by Cook [12, 13], solving the governing equations for species mass density, momentum, and internal energy:

$$\frac{\partial \rho_\alpha}{\partial t} + \nabla \cdot (\rho_\alpha \mathbf{u} + \mathbf{J}_\alpha) = 0 \,, \tag{7}$$

$$\frac{\partial \rho \mathbf{u}}{\partial t} + \nabla \cdot (\rho \mathbf{u}\mathbf{u} + p_i + p_e - \boldsymbol{\tau}_i - \boldsymbol{\tau}_e) = 0 \,, \tag{8}$$

$$\frac{\partial \rho e_i}{\partial t} + \nabla \cdot (\rho e_i \mathbf{u} + \mathbf{q}_i) + p_i \nabla \cdot \mathbf{u} = \boldsymbol{\tau}_i : \nabla \mathbf{u} + \gamma_{ei}(T_e - T_i) \,, \tag{9}$$

$$\frac{\partial \rho e_e}{\partial t} + \nabla \cdot (\rho e_e \mathbf{u} + \mathbf{q}_e) + p_e \nabla \cdot \mathbf{u} = \boldsymbol{\tau}_e : \nabla \mathbf{u} - \gamma_{ei}(T_e - T_i) \,, \tag{10}$$

where ρ_α is the mass density of species α such that $\rho = \sum_\alpha \rho_\alpha$ is the total mass density; $\mathbf{u}$ is the mass-averaged velocity; p_i, T_i, e_i and p_e, T_e, e_e are the ion and electron pressure, temperature, and internal energy per unit mass; and γ_{ei} is the electron-ion coupling parameter. $\mathbf{J}_\alpha$ is the diffusive flux. Radiation effects are not considered in the current application and are negligible at these conditions.

To mimic the fixed electron temperature in the `ddcMD` simulations, a "thermostat" is added to the righthand-side of Eq. (10) in the form $(c_{ve}/\tau_0)(T_0 - T_e)$, where T_0 =1 eV is the target temperature, c_{ve} is the electron specific heat per unit volume, and τ_0 is a relaxation time comparable to the numerical time step. Further, T_i is uncoupled from T_e by setting $\gamma_{ei} = 0$, consistent with the thermodynamic behavior in `ddcMD`.

When the electron temperature is not constrained, there is a pronounced separation of ion and electron temperatures at the shock front due to unequal shock heating of ions and electrons and finite equilibration times; the much higher thermal conductivity of the electrons also broadens the electron temperature profile at the shock front, forming a preheated region ahead of the shock. An example of this is shown later in Section IV A, for which we used the Brysk model for ion-electron coupling coefficient γ_{ei} [35] and the Lee-More electron thermal conductivity model [36] with corrections for electron-electron collisions [37, 38] and with no flux limiting. The MD simulations discussed here lack these distinctly electronic features and in this regard resemble more the MC simulations of neutral atoms (rigid elastic spheres) by Bird [39].

B. Mean Velocity Ion Transport Model

The ion viscous stress is evaluated with Stokes' law $\boldsymbol{\tau}_i = 2\eta_i \mathcal{S}$, where $\mathcal{S}$ is the trace-free strain rate tensor for $\mathbf{u}$ and η_i is the ion viscosity for the mixture. Note that the electron viscosity η_e [40, 41] is much less than η_i because of the small electron mass and low electron temperature, thus $\boldsymbol{\tau}_e = 2\eta_e \mathcal{S}$ is negligible with respect to $\boldsymbol{\tau}_i$ and can be neglected in Eq. (8). The ion species mass fluxes $\mathbf{J}_\alpha$ and ion heat flux $\mathbf{q}_i$ are solved from a coupled linear system using the Chapman-Enskog model [42, 43]. For a binary ion mixture (species α and β), these fluxes are given by

$$\mathbf{J}_\alpha = -\frac{\rho D_{\alpha\beta}}{n_i k_B T_i} \frac{y_\alpha y_\beta}{x_\alpha x_\beta} \left\{ \nabla p_\alpha + z_\alpha \nabla p_e - y_\alpha \nabla p + k_{T\alpha}^{(i)} n_i k_B \nabla T_i + k_{T\alpha}^{(e)} n_e k_B \nabla T_e \right\} , \tag{11}$$

$$\mathbf{q}_i = -\kappa_i \nabla T_i + n_i k_B T_i \sum_\alpha^{N_s} \rho_\alpha^{-1} k_{T\alpha}^{(i)} \mathbf{J}_\alpha + \sum_\alpha^{N_s} h_\alpha \mathbf{J}_\alpha \,, \tag{12}$$

where n_i and n_e are the ion and electron number density; p_α is the partial pressure for ion species α such that

$\sum_\alpha^{N_s} p_\alpha = p_i$; $p = p_i + p_e$ is the total pressure; h_α is the enthalpy per unit mass for ion species α; and $x_\alpha, y_\alpha, z_\alpha$ are the ionic number, mass, and charge fractions for ion species α. The $z_\alpha \nabla p_e$ term comes from the Lorentz force term using Ohm's law (Section VI D). Note that $\mathbf{J}_\alpha = -\mathbf{J}_\beta$, $k_{T\alpha}^{(i)} = -k_{T\beta}^{(i)}$, and $k_{T\alpha}^{(e)} = -k_{T\beta}^{(e)}$. For the present case of an isotopic mixture of hydrogen, there are some simplifications: $p_\alpha = x_\alpha p_i$, $z_\alpha = x_\alpha$, and $k_{T\alpha}^{(e)} = 0$, such that Eq. (11) becomes

$$\mathbf{J}_\alpha = -\frac{\rho D_{\alpha\beta}}{n_i k_B T_i} \frac{y_\alpha y_\beta}{x_\alpha x_\beta} \left\{ p_i \nabla x_\alpha + (x_\alpha - y_\alpha) \nabla p + k_{T\alpha}^{(i)} n_i k_B \nabla T_i \right\} . \tag{13}$$

The driver terms on the righthand-side of Eq. (13) are the usual concentration gradient term (Fick's law), barodiffusion due to mass differences driven here by the *total* pressure gradient, and thermodiffusion (Soret effect) driven by the ion temperature gradient. The heat flux in Eq. (12) is composed of a temperature gradient term (Fourier's law), a thermodiffusion term (Dufour effect), and enthalpy diffusion.

Expressions for the ion transport coefficients — the interdiffusivity $D_{\alpha\beta}$, the ion thermodiffusivity $k_{T\alpha}^{(i)}$, the ion thermal conductivity κ_i, and the ion viscosity η_i — are given in terms of binary collision integrals [42–45]; these all correspond to 1st approximation in the Chapman-Enskog kinetic theory, except for interdiffusivity, which is 2nd approximation. Curve fits for binary collision integrals for static screened Coulomb (Yukawa) potentials are given by Paquette *et al.* [44] and Stanton and Murillo [45], and here we use the definition of screening length for a mixture suggested by the latter authors.

At the conditions simulated here a different approach is needed for the viscosity model. The plasma is moderately coupled, and the Chapman-Enskog model accounts only partially for viscosity. Instead, we use a generalization that transitions smoothly from the Chapman-Enskog model [43, 44] in the weakly coupled limit to the Yukawa Viscosity Model [46] in the strongly coupled regime. The model, known as the Kinetic Molecular Dynamics (KMD) viscosity model [20], captures this transition in the following form:

$$\eta_{KMD} \approx ([\eta]_{CE}^2 + \eta_{YVM}^2)^{1/2} . \tag{14}$$

The model η_{YVM} is an analytic form fit to moderately and strongly coupled MD results for the viscosity of Yukawa plasma [46]. The KMD viscosity model represents in an approximate fashion contribution of the kinetic, potential, and cross terms of viscosity.

C. Mixture equation of state (EOS)

In general, for given species mass densities and internal energy, an equilibrium is found for the mixture in which each species has the same total pressure and ion temperature as described by [47] using tabular EOS data. Here we treat isotopic (hydrogenic) species so that a single SESAME EOS table for hydrogen is used with appropriate mass scalings [48]. The charge states for given density and electron temperature are determined from a fit to the Thomas-Fermi model [49]. At the high densities and low temperatures used in this study the electrons are highly degenerate; the cold-curve (zero temperature) pressure is the dominant component of pressure in the mixture ahead of shock, while the thermal component of ion pressure is the dominant component of pressure in the hot post-shock region. With $T_e = 1$ eV everywhere, the contribution from the thermal electron pressure is negligible.

D. Jump Conditions

The Rankine-Hugoniot jump conditions for a steady planar shock are found by equating the pre-shock and post-shock values of one-dimensional mass, momentum, and total energy fluxes in the frame of the shock [50]; it is assumed that the species mass flux, stress, and heat flux vanish in these regions. Throughout the rest of this manuscript, we denote quantities derived in the regions far ahead of the shock with "–" and far behind the shock with "+". From mass conservation, the total mass flux (momentum) ρu in the frame of the shock is a constant j related to the piston speed u_p and the shock speed u_s by

$$j = \rho_- u_s = u_p / (1/\rho_- - 1/\rho_+) . \tag{15}$$

Here we also assume $y_{\alpha-} = y_{\alpha+}$, i.e., the same species concentrations on either side of the shock. The other relations are in terms of the shock momentum j

$$j^2/\rho_- + p_- = j^2/\rho_+ + p_+ , \tag{16}$$

$$e_- + (j^2/2\rho_- + p_-)/\rho_- = e_+ + (j^2/2\rho_+ + p_-)/\rho_+ , \tag{17}$$

or in terms of the piston speed u_p

$$(p_+ - p_-)(1/\rho_- - 1/\rho_+) = u_p^2 , \tag{18}$$

$$e_+ - e_- - p_-(1/\rho_- - 1/\rho_+) = u_p^2/2 . \tag{19}$$

Because the total internal energy per unit mass e is a function of total pressure p and mass density ρ, implicitly defined by the equation of state, these relations specify all of the thermodynamic jump conditions in terms of the imposed piston speed. The Mach number is given by $M = u_s/c_{s-} = j/(\rho c_s)_-$, where c_s is the sound speed. We typically find that the density and pressure jump conditions are similar to those predicted by a monatomic perfect gas with polytropic index $\gamma = 5/3$ for the same Mach number, but the relative temperature jump across the shock is much greater. This disparity is a bit misleading, as the actual temperature behind these strong shocks is fairly consistent with a $\gamma = 5/3$ perfect gas using $e_+ \approx u_p^2/2 \approx 3k_B T_i/2m$ (where m is the mean mass); however, the pressure and internal energy ahead

of the shocks is dominated by the non-thermal components, which in an ideal gas would require a much higher temperature (and lower relative temperature jump) to match.

The comparison of jump conditions in Table I shows that the ddcMD simulations results agree much closer with those from the SESAME EOS than with those from an ideal $\gamma = 5/3$ gas. This provides some confidence that the EOS used in the continuum code is a fair representation of the ddcMD thermodynamics. Note that the Hugoniot $u_s - u_p$ relation is fairly insensitive to the isotopic mixture in both the MD simulations and the continuum simulations using the SESAME EOS, so the Mach number shown in Table I is roughly proportional to the square root of the average mass. The sound speed was not directly calculated from the ddcMD simulation results, but it seems reasonable to assume that these Mach numbers are equivalent to those in the MD simulations given the good agreement of the shock speeds and the other jump conditions.

E. Simulation setup

One-dimensional continuum simulations are initialized with the jump conditions in Table I for a given post-shock (piston) velocity at an extended distance from the wall rather than using an actual piston. An initial transient is generated when the light isotope becomes enhanced in the shock, forming a commensurate enhancement of the heavy isotope behind the shock due to species number conservation. Given enough time, the shock outruns the trailing transient, leaving a flow immediately behind the shock that has nearly the original homogeneous composition and satisfies the originally predicted thermodynamic jump conditions. For a fixed piston speed we observe that the greater the mass disparity between isotopes, the higher the Mach number of the shock and the more distance needed for the shock to outrun the trailing transients — both in Miranda and ddcMD simulations. For the 1:3 mass ratio, the shock can be started at a distance of 100 nm from the wall, while for the 1:20 mass ratio the shock required at least 1000 nm. Miranda grid spacings of 0.1 nm for mass ratios ≤ 10 and 0.2 nm for higher mass ratios are used, which are adequate to resolve the post-shock structure where macroscopic mean free paths, defined with ion transport coefficients, are typically greater than 0.5 nm (see Table IV and associated discussion) but inadequate to resolve the shock front, where the local mean free path drops ahead of the shock by two orders of magnitude, leading to Gibbs oscillations in the numerical solution there.

IV. RESULTS

A. General Shock Structure

Typical mean ion temperature, pressure, mass density, and species number fraction profiles for MD and continuum calculations are shown for a ^{1}H-^{3}H case in Fig. 2. The jump in ion temperature precedes the jump in the other quantities shown and the number fraction of the lighter species is enhanced at the shock front, which is typical of shock structure in mixtures. In this case the shock has had time to outrun the trailing transient. Comparisons of MD and continuum number fraction and number density profiles are shown for the ^{1}H-^{3}H case in Fig. 3. The overall amount of separation (the induced change in number fraction) is comparable between the Miranda and ddcMD results, but the shape of the separation feature and the detailed shock structure are noticeably different. In particular, the continuum code treats the ion transport coefficients and mean free path as local functions of thermodynamic variables, which drop two orders of magnitude across the shock (ahead of the shock), causing an unphysically sharp shock front. Like its ddcMD counterpart, the front is led by the lighter species. Indeed, a hallmark of non-dissipative shocks in the continuum description is that the flow is completely unaware of the oncoming shock. The MD separation feature is observed to be markedly broader and more symmetric than the continuum one in Fig. 3. Most notably, the separation feature leading the MD shocks is longer than that trailing the shock. This separation ahead of the shock is completely absent in continuum results. The broader trailing "shock" in the heavy component lies in the hot region of the shock with longer mean free paths and is captured more accurately by the continuum code. Note that this continuum code is not constitutionally capable of handling different ion temperatures observed in multifluid analyses of shock structure in mixtures [51], nor the additional kinetic effects observed in the MD simulations here and by previous authors [52], in PIC simulations [2], and in MC simulations [16, 39, 53, 54].

Figure 4 compares species and mixture temperatures obtained with ddcMD to the continuum mixture temperature for a shock in an equimolar H-T mixture. It is evident by comparing to Fig. 3 that for ddcMD the temperature rise in the light species leads the jump in density by a distance of approximately 5 nm. Ahead of the shock, the temperature of the light species is higher than both the mixture and the heavy species temperatures. Within the shock, the temperature of the heavy species overshoots the mixture and light species temperatures, while the temperature of the light species experiences no such overshoot, monotonically increasing across the shock. Behind the shock, all temperatures eventually relax to the same post-shock value. Continuum multifluid models [19, 51] show a similar overshoot in heavy species temperature (see discussion in Section V B).

A case where electron temperature is not constrained is shown in Figure 5 for the H-T shock with a Mach num-

TABLE I. Jump conditions for equimolar hydrogenic mixtures: $T_- = 1$ eV, $n_{i-} = 1024$ nm^{-3}, $u_p = 80$ nm/ps; $\gamma = 5/3$ conditions for the same Mach number M; numbers in *italics* are estimated from unsteady conditions; u_s in nm/ps; n_{i+} in nm^{-3}.

	Miranda/SESAME EOS						$\gamma = 5/3$			ddcMD		
mixture	M	u_s	n_{i+}	ρ_+/ρ_-	T_+/T_-	p_+/p_-	ρ_+/ρ_-	T_+/T_-	p_+/p_-	u_s	ρ_+/ρ_-	T_+/T_-
^{1}H-^{3}H	4.91	113	3476	3.39	36.2	30.8	3.56	8.40	29.9	112.5	3.38	38
^{1}H-^{5}H	5.90	111	3648	3.56	57.2	44.9	3.68	11.7	43.3	111.1	3.6	59
^{1}H-^{10}H	7.83	109	3840	3.75	110	79.9	3.81	20.0	76.4	*110*	*3.75*	*115*
^{1}H-^{15}H	9.38	108	3920	3.83	165	115	3.87	28.4	110	*109*	*3.8*	*170*
^{1}H-^{20}H	10.7	108	3964	3.87	219	150	3.90	36.6	143	*109*	*3.85*	*240*

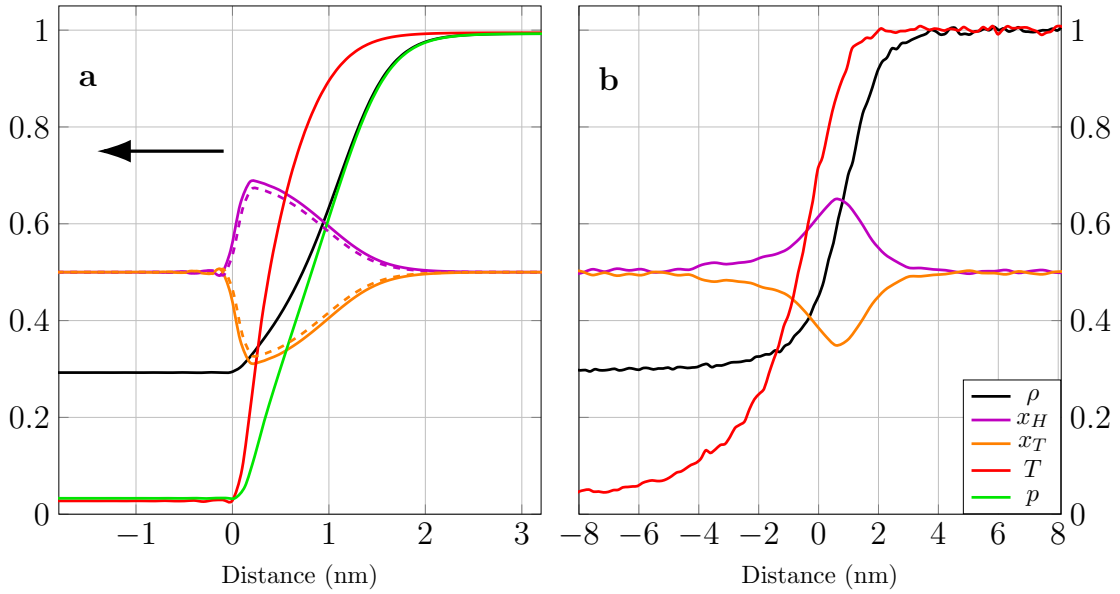

FIG. 2. Profiles of thermodynamic variables (normalized to their maxima) and number fractions around the shock in an equimolar ^{1}H-^{3}H (H-T) mixture with $n_i = 1024$ nm^{-3} from continuum (**a**) and MD (**b**) calculations. Here and in the following H-T plots the Mach number is M=4.91. The shock proceeds in the direction of the arrow. Dashed lines show the number fractions in the absence of thermodiffusion. The pressure was not calculated for the MD simulations. In particular, note the difference in length scales for the two sets of results.

ber of 4.9. There are three noteable differences compared with the cases where the electron temperature is held at 1 eV: (1) The jump in temperature across the shock is lower as electrons can carry more of the thermal energy in the shocked plasma. (2) The ion temperature at the shock front overshoots the post-shock temperature; this occurs because ions are heated by the shock more than electrons, and it takes a distance of about $c_{pi}u_s/\gamma_{ei} \approx 10$ nm for the temperatures to equilibrate behind the shock (where c_{pi} is the ion specific heat per unit volume, u_s is the shock speed, and γ_{ei} is the electron-ion coupling coefficient in Eq. 10). (3) The high electron thermal conductivity in the shocked plasma heats the electrons well ahead of the shock and the thermal coupling from ion-electron collisions in turn warms the ions there, giving a foot in the ion temperature profile preceding the shock. In addition, lower temperatures and broadened temperature profiles lead to lower species separation but no significant change in the ion shock width. The overshoot of the mean ion temperature in this case is analogous to the overshoot observed in the temperature of the heavy ion species in the MD simulations. While the thermal precursor due to electron heating bears some resemblance to the ionic preheating seen in the MD simulations, the latter exceeds what can explained by the low ion thermal conductivity predicted by the transport model.

B. Ion viscosity

Viscosity can have a significant effect on shock front structure, increasing the shock thickness qualitatively, much like other dissipative and kinetic effects do. We are relying on continuum modeling with the KMD vis-

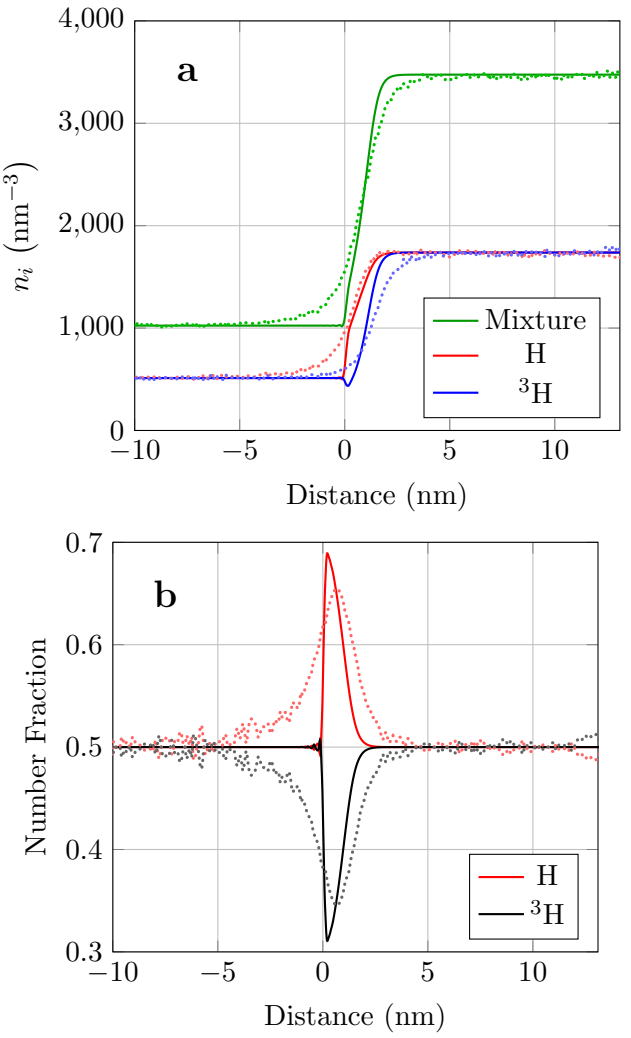

FIG. 3. Mixture number density and density of individual species for a shock wave in an H-T mixture (**a**). Number fraction of individual species for a shock wave in an H-T mixture (**b**). Dots represent MD results and solid lines represent continuum results.

cosity model Eq. (14) to assess the size of those effects. We could also tune the viscosity to get agreement with the observed shock thickness. This kind of analysis motivates some questions. How accurately do we know the viscosity? Does the viscosity model used in the continuum simulations agree with the viscosity of the MD-simulated plasma? The continuum simulations are using an advanced viscosity model [20], but the model has not been used or tested in this regime previously. In this section we compare the predictions of the KMD viscosity model with the viscosity computed directly from MD for thermodynamic conditions that correspond to the pre-shock stage at $T = 1$ eV and $n_i = 1.024 \times 10^{24}$cm^{-3} and 50% mixture of H isotopes with mass ratio; 1:3, 1:5, 1:10, 1:15 and 1:20. In the comparison above we have seen that the leading edge of the shock is much sharper in the continuum simulations than in MD. The trailing side of the shock profile is in better agreement. By com-

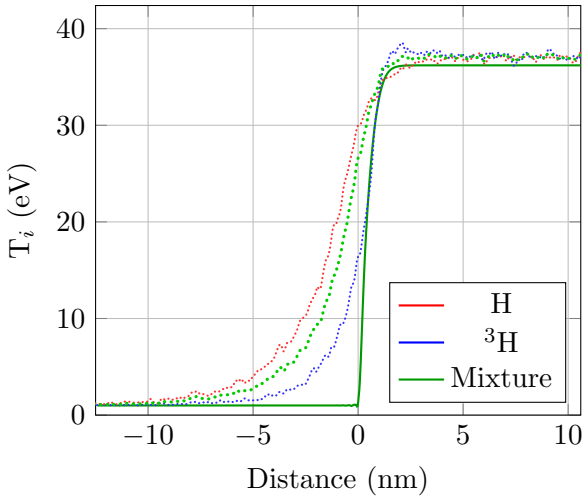

FIG. 4. Species ion temperature in the vicinity of the shock for an H-T mixture. Dots represent MD results and solid lines represent continuum results.

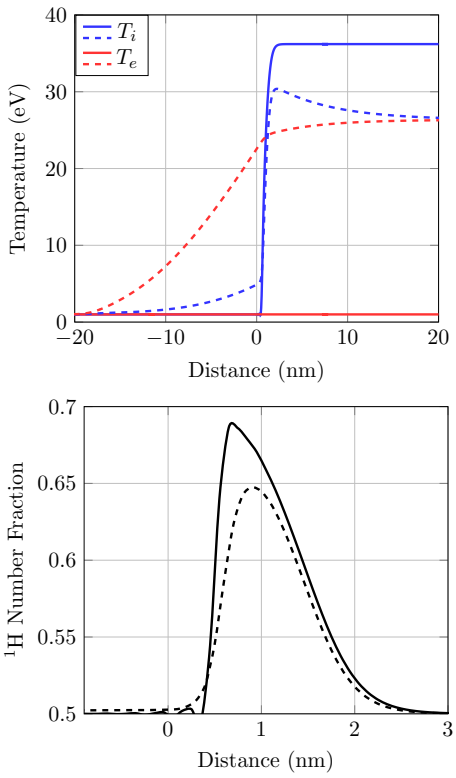

FIG. 5. Temperature and number fraction profiles from continuum simulations in the vicinity of a Mach 4.9 shock in an H-T mixture with electrons held at 1 eV (solid lines) and with unfettered ion-electron equilibration (dashed lines).

puting the viscosity from MD directly, we can investigate whether the difference in the leading edge is due to differences in the viscosities at these conditions.

We have computed shear viscosity directly using equilibrium molecular dynamics. These calculations use smaller systems than the shocks, equilibrated at the

pre-shock conditions, and then run at equilibrium long enough to collect the statistics needed to evaluate the viscosity using a fluctuation-dissipation relation. The pre-shock region far ahead of the shock front is in local thermodynamic equilibrium (LTE). Therefore in this focused MD study we can make use of the Green-Kubo (GK) approach to extract linear transport coefficients. GK formulas are fluctuation-dissipation relations, expressing a macroscopic phenomenological transport coefficient, like viscosity, as a time integral of a microscopic time-correlation function for systems undergoing small fluctuations around thermodynamic equilibrium. For shear viscosity we use the stress autocorrelation function (SAF) defined in the center-of-mass frame as:

$$J_{xy}^{stress}(t) = \langle \mathcal{S}_{xy}(0)\mathcal{S}_{xy}(t)\rangle, \tag{20}$$

where $\langle\cdots\rangle$ represents a statistical ensemble average. The off-diagonal terms of the stress tensor $\mathcal{S}_{xy}$ are given by

$$\mathcal{S}_{xy} = -\frac{1}{V_{tot}}\left(\sum_{a=1}^{N} m_a v_{x,a} v_{y,a} + \sum_a \sum_{b>a} \frac{r_{ab}^x r_{ab}^y V'(r_{ab})}{r_{ab}}\right), \tag{21}$$

where x and y denote Cartesian coordinates, m_a is the mass of ion a and r_{ab} the distance between ions a and b, and V_{tot} the total volume of the system. The interaction force between ions a and b enters in the second term through $V'(r) \equiv dV/dr$. The first term of the stress tensor on the right hand side of Eq. (21), $\mathcal{S}_{xy,kin} = V_{tot}^{-1}\sum_{a=1}^{N} m_a v_{x,a} v_{y,a}$, is a kinetic contribution that represents transverse momentum transfer by ion displacement [50, 55]. This term is important in weakly coupled plasma. In practice, we average over the five independent components of shear stress to get better convergence [56].

The Green-Kubo formula for shear viscosity is

$$\eta_i = \lim_{t\to\infty} \frac{1}{nk_BT}\int_0^t d\tau J_{xy}^{stress}(\tau). \tag{22}$$

As previously mentioned this GK approach is appropriate to use when the shear strain rate is small compared to the the reciprocal of the shear stress correlation time, which is true for regions far from the shock front. Since our MD simulations only have dynamic ions, not dynamic electrons, the Green-Kubo formula gives the ionic viscosity. The electronic viscosity at these conditions is small, and is absent from both the MD and continuum simulations.

At temperature $T = 1$ eV and ion density $n_i = 1.024 \times 10^{24}\text{cm}^{-3}$, the mean charge from the Thomas-Fermi approach is $\overline{Z} = 0.7324$ and the electron density is $n_e = 7.499 \times 10^{23}\text{cm}^{-3}$. The mixture is moderately coupled with Coulomb coupling coefficient $\Gamma = (\overline{Z}e)^2/a_i k_B T = 12.55$, where $a_i = (3/4\pi n_i)^{1/3} = 0.0615$ nm is the interion distance (Wigner-Seitz radius). The electrons are highly degenerate at these conditions, i.e., the Fermi energy $\varepsilon_F = \hbar^2(3\pi^2 n_e)^{2/3}/2m_e \gg k_B T_e$, and the Debye length is given to good accuracy by $\lambda_{De} \approx (\varepsilon_F/6\pi n_e e^2)^{1/2} = 0.0384$ nm, which in turn gives an electron screening coefficient $\kappa = a_i/\lambda_{De} = 1.602$.

In Table II we show values of η_i as computed from MD using GK approach. Also in the same table we provide values of viscosity extracted from the KMD model η_i^{KMD}. For comparison we include values of viscosity computed using Chapman-Enskog (CE) kinetic theory. We use tabulated collision integrals [44], with an effective screening [20] that interpolates between interion distance and total particle screening length to extract η_{CE}. Also, we report viscosity η_{SM} calculated using a different approach for the effective screening due to [45] that gives somewhat larger values than η_{CE} at moderate to high coupling. The differences in these two kinetic models manifest themselves in a physical regime where collective effects and particle correlations, that in general are not accurately captured by binary collision approaches, become important, and kinetic models in this regime are subject to some uncertainty.

As demonstrated in Table II, the KMD model is in very good agreement with the values computed from MD; i.e., the values of η_i^{MD} and η_i^{KMD} agree to better than 15%. The differences would have a negligible effect on the shock profile.

TABLE II. Shear viscosity values η_i^{MD} computed from MD for binary mixtures of H and its isotopes of different masses at $T = 1$ eV and ion density $n_i = 1.024 \times 10^{24}\text{cm}^{-3}$. For comparison, we also present values of viscosity from models as described in the text. All shear viscosity values are given in units of mPa·s.

Mixture	η_i^{MD}	η_i^{KMD}	η_{CE}	η_{SM}
^{1}H-^{3}H	0.997	1.04	0.301	0.707
^{1}H-^{5}H	1.22	1.28	0.378	0.889
^{1}H-^{10}H	1.52	1.74	0.534	1.26
^{1}H-^{15}H	2.11	2.01	0.662	1.56
^{1}H-^{20}H	2.46	2.41	0.774	1.83

V. BARODIFFUSION AND SPECIES SEPARATION

As the mass ratio of species in the mixture is increased, the effects of barodiffusion and species separation become more pronounced. When tritium is replaced by successively heavier hydrogen isotopes, the heavy species responds to the pressure gradient more sluggishly. As seen in Fig. 6, this leads to an increased shock thickness. In the most extreme cases, the shock in the light species leads that in the heavy species by nearly 30 nm. At this level of separation, two distinct density jumps are clearly visible in the mixture, leading to a "shoulder" structure in the mixture density at the shock. Continuum simulations also predict this shoulder structure,

though the leading light-ion shock front remains significantly sharper than MD results. The peak separation in number fraction in the ddcMD results is observed to be less than 0.18 for steady cases in Fig. 7 and in Table III, although the shock has clearly not outrun the transients in the cases with mass ratio ≥ 10. The amount of species separation due to barodiffusion and its effect on the shock width is examined here in the context of continuum models, which provide a basis for understanding some of the underlying physics.

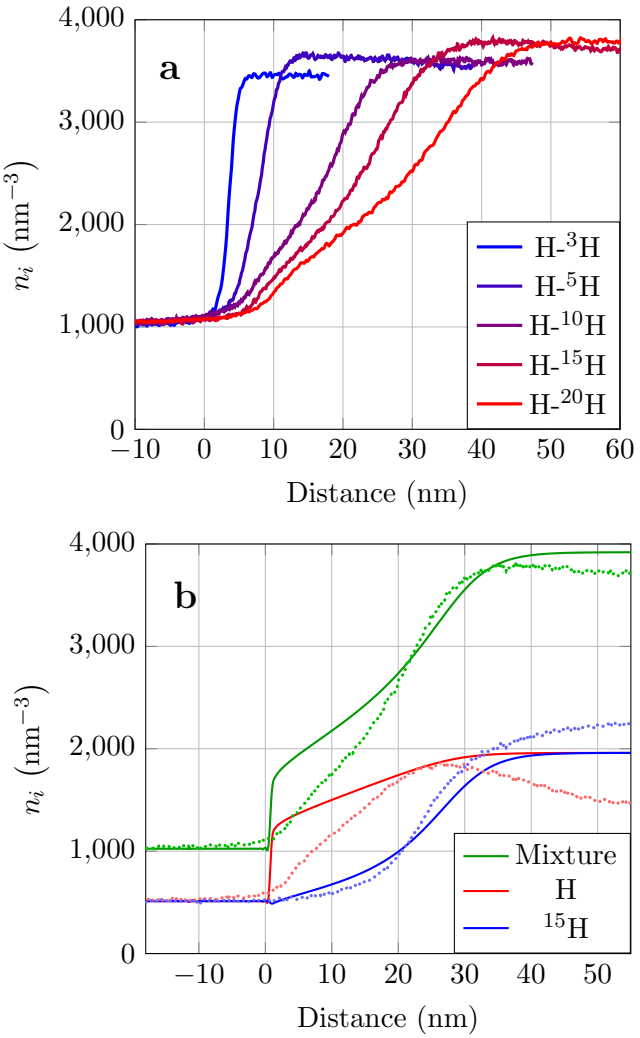

FIG. 6. Mixture number density profiles for MD shocks in mixtures with increasingly disparate mass ratios (**a**) and a comparison of species number densities from MD and continuum simulations for the H-^{15}H case (**b**). In the comparison, MD results are represented with dots and continuum is represented with a solid line.

A. 1D single-fluid continuum model

The steady planar shock structure predicted by the continuum code, using a single fluid velocity and single ion temperature, can be determined in principle by setting the species mass flux, stress, and total energy flux to constants in the frame of the shock including diffusion, viscous stress, and heat conduction terms. This results in a coupled, highly nonlinear set of ODEs whose length scales depend on ion diffusivity, viscosity, and thermal conductivity; in general the easiest way to solve these equations numerically is to wait for the continuum PDE solution to reach a steady state, although this affords little analytical insight. It is the species mass flux, $\rho_\alpha u + J_\alpha = j y_\alpha + J_\alpha = j y_{\alpha\pm}$, that governs the species separation properties in the continuum equations:

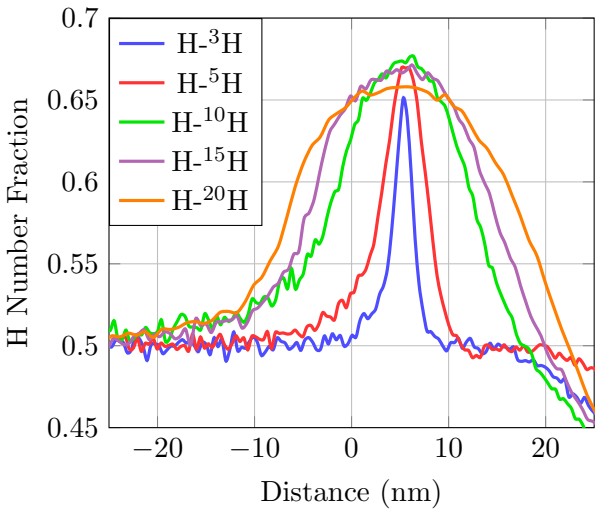

FIG. 7. H Number fractions from MD simulations for a variety of mass ratios.

TABLE III. Maximum species separation $\Delta x = |x_j - x_{j\pm}|$ (values from ddcMD in *italics* are approximated from unsteady conditions) and maximum relative overshoot of heavy-species temperature $\Delta T = T_n/T_+ - 1$. The first Miranda value uses the local ion temperature in the ion transport coefficients, while the second uses the post-shock ion temperature everywhere.

	ideal multifluid		Miranda		ddcMD
mixture	Δx	ΔT	$\Delta x(T_i)$	$\Delta x(T_{i+})$	Δx
^{1}H-^{3}H	0.108	0.011	0.188	0.151	0.156
^{1}H-^{5}H	0.137	0.012	0.208	0.172	0.176
^{1}H-^{10}H	0.162	0.014	0.211	0.179	*0.176*
^{1}H-^{15}H	0.168	0.016	0.211	0.180	*0.175*
^{1}H-^{20}H	0.171	0.018	0.211	0.181	*0.155*

$$y_\alpha - y_{\alpha\pm} \approx \lambda_D \left\{ \partial y_\alpha + \frac{y_\alpha y_\beta}{x_\alpha x_\beta}(x_\alpha - y_\alpha)\left(\frac{\partial p}{p} + \theta_i \frac{\partial T_i}{T_i}\right)\right\}, \tag{23}$$

where ∂ denotes the spatial derivative, $\lambda_D \equiv \rho D/j$ is the shock diffusion length, $D = D_{\alpha\beta}(p/n_i k_B T_i)$, and

$\theta_i(x_\alpha - y_\alpha) = k_{T\alpha}^{(i)}(n_i k_B T_i/p)$; or

$$x_\alpha - x_{\alpha\pm} \approx \lambda_D \frac{m_\pm}{m}\left\{\partial x_\alpha + (x_\alpha - y_\alpha)\left(\frac{\partial p}{p} + \theta_i \frac{\partial T_i}{T_i}\right)\right\} \tag{24}$$

for $m = x_\alpha m_\alpha + x_\beta m_\beta$ and $y_\alpha = m_\alpha x_\alpha/m$.

Here we ignore the distinction between total pressure and ion pressure to simplify the analysis. If there were no mass difference between the species, the latter terms involving pressure and temperature gradients would vanish, leaving only the concentration gradient and an ODE of the form $y_\alpha - y_{\alpha\pm} = \lambda_d \partial(y_\alpha - y_{\alpha\pm})$, whose only physical solution is trivial, $y_\alpha = y_{\alpha\pm}$, i.e., no species separation.

The sign of the prefactors on the pressure and temperature gradient terms tend to be the same in hot plasmas, so that across a shock both terms act in concert to generate separation. We can assess the contribution of ion thermodiffusivity in `Miranda` by performing simulations in which the ion thermodiffusivity coefficient θ_i is set to zero — something that cannot be done in the `ddcMD` simulations. While values of θ_i from the CE model are roughly 0.3–0.6 behind the shock, the peak pressure and temperature gradients in the shock do not coincide spatially, and the temperature gradient term is found to contribute only 10–20% of the overall species separation (see dashed lines in Fig. 2). For smaller mass ratios thermodiffusivity contributes to both the peak amount of separation and the width of the separation feature; for larger mass ratios the peak amount of separation appears to asymptote to a maximum value of 0.21, as seen in Fig. 8, and thermodiffusivity only affects the width of the separation feature.

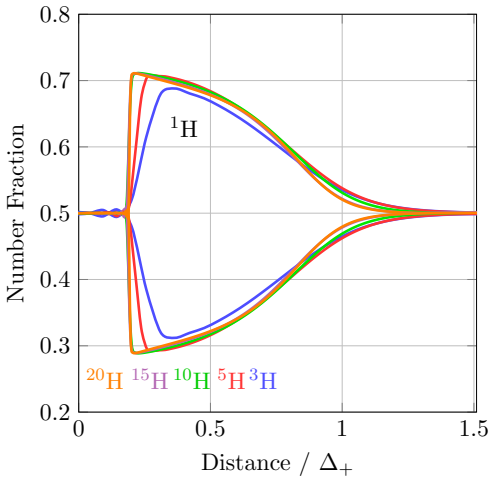

FIG. 8. Number fractions from continuum simulations in the initial shock in equimolar ^{1}H-^{n}H mixtures with $n_i = 1024\ \mathrm{nm}^{-3}$ plotted against distance scaled by Δ_+ from Eq. (25) with arbitrary offsets; the curves for mass ratios ≥ 10 lie nearly on top of each other.

A maximum in species separation is a consequence of the mathematical form of Eqs. (23) and (24): At peak separation, ∂x_α vanishes and Eq. (24) can be approximated by $m(x_\alpha - x_{\alpha\pm}) = m_\pm(x_\alpha - y_\alpha)\phi$, which is cubic in x_α with the parameter $\phi = \lambda_D(\partial \ln p + \theta_i \partial \ln T_i)$. For large enough mass asymmetry, there is an upper limit on both ϕ and $\Delta x_\alpha = x_\alpha - x_{\alpha\pm}$ required for a physical solution; in the limit $m_\beta/m_\alpha \to \infty$, the requirement is $\phi \leq \phi_c = (1 - x_{\alpha\pm}^{1/2})/(1 + x_{\alpha\pm}^{1/2})$ corresponding to $\Delta x_\alpha \leq \Delta x_{\alpha c} = x_{\alpha\pm}^{1/2}(1 - x_{\alpha\pm}^{1/2}) \leq 1/4$. In the cases considered here, $x_{\alpha\pm} = 1/2$, giving $\phi_c = 0.172$ and $\Delta x_{\alpha c} = 0.207$. For large enough mass ratios the continuum model gives nearly discontinuous pressure and temperature jumps with very large gradients that assure the critical value ϕ_c is always attained, probably accounting for the observed behavior. The peak separation in number fraction in the `ddcMD` results is observed to be less than 0.18 for steady cases in Fig. 7 and Table III, which is lower than in the continuum code; the separation features are observed to be broader and more symmetric in Fig. 7, so that this asymptotic state is presumably not attained.

The extent of the separation feature depends not only on the diffusivity but also on the shape of the pressure and temperature profiles in the shock, which in turn depend on the viscosity and thermal conductivity. Macroscopic length scales can be constructed from the ion transport coefficients and the shock momentum j, namely $\lambda_d = \rho D_{\alpha\beta}/j$, $\lambda_D = \rho D/j$, $\lambda_\nu = 4\eta_i/3j$, and $\lambda_\chi = \kappa_i/j c_{pi}$ where c_{pi} is the ion specific heat per unit mass, and the ratios $\mathrm{Sc} = 3\lambda_\nu/4\lambda_d$, $\mathrm{Pr} = 3\lambda_\nu/4\lambda_\chi$, and $\mathrm{Le} = \lambda_\chi/\lambda_d$ give the Schmidt, Prandtl, and Lewis numbers, respectively. The length scale $\lambda_i = 4\eta_i/3\rho c_s$ is often associated with the ion mean free path and the width of the shock in a single-species fluid. Post-shock values of these length scales from the `Miranda` simulations are given in Table IV and compared with the measured widths of the ion number density n_i profile across the shock from `ddcMD` and `Miranda` simulations, defined as the distance between $1.2n_{i-}$ and $0.9n_{i+}$ [2]. For *weak shocks* in a binary γ-law perfect gas mixture, Refs. [14], [15], and [57] derived a shock width from equations like Eq. (12) and Eq. (13), which results in a linear combination of diffusive, viscous, and conductive length scales:

TABLE IV. Post-shock length scales and shock widths in the continuum simulations for equimolar hydrogenic mixtures with $n_{i-} = 1024$ nm^{-3}; all lengths given in units of nm. Some representative pre-shock lengths scales are also given. $\Delta_{\rm MD}$ and $\Delta_{\rm Mir}$ are calculated from the width of the ion number density profile [2], and Δ_+ is calculated from Eq. (25) downstream of the shock. For comparison, the Debye lengths are $\lambda_{De+} = 0.0301$ nm and $\lambda_{De-} = 0.0384$ nm and the inter-ion spacings are $a_{i+} = 0.0392$ nm and $a_{i-} = 0.0615$ nm.

mixture	M	λ_{d+}	λ_{D+}	$\lambda_{\nu+}$	$\lambda_{\chi+}$	λ_{i+}	$\Delta_{\rm MD}$	$\Delta_{\rm Mir}$	$\Delta_{\rm Mir+}$	Δ_+
^{1}H-^{3}H	4.91	0.531	0.846	0.406	0.553	0.196	3.0	1.4	2.4	2.21
^{1}H-^{5}H	5.90	1.15	1.61	0.737	1.08	0.348	6.8	3.5	6.3	5.79
^{1}H-^{10}H	7.83	3.84	4.71	1.89	3.08	0.871	*18.0*	13.1	24.8	23.4
^{1}H-^{15}H	9.38	8.30	9.62	3.47	6.14	1.59	*23.4*	29.1	55.2	54.8
^{1}H-^{20}H	10.7	14.6	16.4	5.46	10.3	2.48	*30.8*	53.6	97	102

mixture		λ_{d-}	λ_{D-}	$\lambda_{\nu-}$	$\lambda_{\chi-}$	λ_{i-}			Δ_-
all		0.003	0.020	0.003	0.003	0.021			0.022–0.042

$$\Delta = \frac{4\gamma}{\epsilon(\gamma+1)} \left\{ \lambda_\nu + (\gamma-1)\lambda_\chi + \gamma x_\alpha x_\beta \lambda_D \left(\frac{m_\beta - m_\alpha}{m} \right)^2 \left(1 + \frac{\gamma-1}{\gamma}\theta_i \right)^2 \right\} , \tag{25}$$

where $\epsilon = \gamma(M^2-1)/(\gamma M^2+1) \approx 1$, which in these references was evaluated ahead of the shock. Also note that this shock width is derived from $u_p/u'_{\rm max}$ where $u'_{\rm max}$ is the maximum slope of the mean ion velocity profile; this is comparable to Bellei's [2] definition for fairly symmetric shock structure, but can give quite disparate results in highly asymmetric cases. In the continuum results, θ_i ranges from 0.3 to 0.6 behind the shock and is about 0.1 ahead of the shock; and the ratio of specific heats for ions γ_i ranges from 1.3 to 1.6 behind the shock and is about 1.1 ahead of the shock. For a strong shock, it may make more sense to evaluate this expression using values behind the shock; post-shock values Δ_+ are given in Table IV, where it is seen that the species separation term in Eq. (25), proportional to the diffusion width λ_D, is the dominant term for even modest mass ratios. Figure 8 shows that Δ_+ provides quite good scaling for the width of the separation feature in the continuum simulations for all mass ratios, although it overestimates these widths by nearly a factor of 2. On the other hand, Δ_+ does very poorly at scaling the `ddcMD` results (Fig. 7) and greatly overestimates the shock width at large mass ratios. For lower mass ratios and Mach numbers, the width of the shock in the `ddcMD` simulations $\Delta_{\rm MD}$ is twice that in the `Miranda` simulations $\Delta_{\rm Mir}$; at high mass ratios and Mach numbers, the situation is reversed. Some of this discrepancy may be due to the proximity of the shock to the piston in the high-mass-ratio `ddcMD` simulations, which may be compressing the shock; if the shock were to achieve greater separation from the piston in these cases, it is possible that the steady-state structure would be more elongated, but it is doubtful that it would be enough to change the general result.

Particle-in-cell (PIC) simulations [2] for shocks in a D-T plasma, including thermal broadening by electron conduction, show a marked decrease in the ratio of shock width to post-shock mean free path Δ_s/λ_{i+} for Mach numbers greater than 6, and it is interesting that a similar decline in Δ_s/λ_{i+} is observed for Mach numbers greater than 8 in the MD simulations presented in this study with fixed electron temperature. This behavior is not predicted by continuum and kinetic models of strong shocks in single-species plasmas [58, 59] that account for electron preheating, nor in the weak-shock model for binary mixtures [14], nor in continuum simulations, all of which suggest that Δ_s/λ_{i+} should approach a constant asymptotic value for strong steady shocks moving through a medium *with fixed composition*, i.e., when the Mach number M is increased only by increasing the piston speed u_p. For example, in `Miranda` continuum simulations including electron preheating (cf. Fig. 5) with fixed heavy-to-light mass ratio $m_2/m_1 = 3$, Δ_s/λ_{i+} increases only from 16 to 19 for $u_p = 80$ to 180 nm/ps ($M = 4.9$ to 10.5), whereas when u_p is fixed at 80 nm/ps and m_2/m_1 increases from 3 to 20 ($M = 4.9$ to 10.7), Δ_s/λ_{i+} increases from 16 to 90 almost linearly with M. A linear growth of Δ_s/λ_{i+} with Mach number is also seen in the `Miranda` results for fixed electron temperature and fixed u_p in Table IV. This result can be understood by examining the weak-shock formula in Eq. (25), which does a good job scaling the continuum shock width. The viscous term $\lambda_{\nu+}/\lambda_{i+} = (\rho c_s)_+/j$ is roughly constant (about 2) for the range of Mach numbers considered here ($M = 5$ to 11), and in fact it attains a maximum value of $\sqrt{5}$ for an infinite mass ratio or an infinite strength shock in a $\gamma = 5/3$ perfect gas. In contrast, the ratios for species diffusion $\lambda_{D+}/\lambda_{i+}$ and thermal conductivity $\lambda_{\chi+}/\lambda_{i+}$ steadily increase with increasing mass ratio roughly as a linear function of $(m_2/m_1)^{1/2}$. For fixed u_p, M also scales as $(m_2/m_1)^{1/2}$, hence Δ_s/λ_{i+} should grow as a linear function of increasing M, rather than decrease as observed in the MD results for strong shocks. The

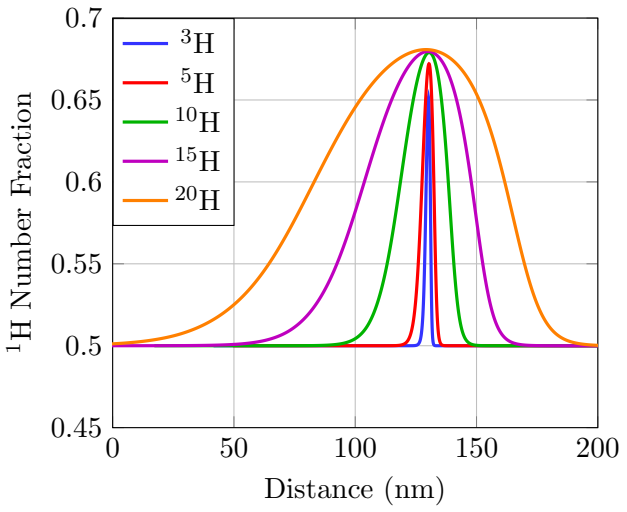

FIG. 9. Number fractions from continuum simulations in which the post-shock temperature is used to calculate the ion transport everywhere. Note that the scale of the abscissa is 4 times larger than in Fig. 7.

turnover in Δ_s/λ_{i+} observed in both PIC and MD simulations at high Mach numbers is not yet understood, but it may be the result of highly nonlinear, non-equilibrium effects not captured in continuum models. Given the differences in species composition, thermodynamic conditions, and the treatment of electrons in these various studies, it's difficult to make a sensible quantitative comparison of actual ion shock widths.

The local transport coefficients and their associated length scales drop abruptly by two orders of magnitude, giving a nearly discontinuous shock front not seen in the MD simulations. In order to demonstrate (in a crude fashion) the effect of enhanced, non-local transport in the vicinity of the shock, another set of continuum simulations was performed using the post-shock ion temperature at all points in the flow to calculate the ion transport coefficients, making them fairly uniform. (Caveat: This is a very case-specific artifice that should not be construed as a practical general model.) The species number separation is shown for this case in Fig. 9, where much more symmetric shock profiles are obtained, more consistent in shape with the `ddcMD` profiles in Fig. 7 and in peak number fraction in Table III. The shock widths from this test case agree even better with the weak shock formula Eq. (25) ($\Delta_{\rm Mir+}$ in Table IV); but this only improves the agreement with the `ddcMD` results at small mass ratios, while making the agreement even worse for larger ones.

Continuum and kinetic models [58–60] *for a fixed composition* typically show that the width of the ion shock Δ_s as a function of Mach number M approaches a constant multiple of the post-shock ion mean free path λ_{i+} as $M \to \infty$, regardless of electron preheating. However when the piston speed u_p is fixed and the Mach number increases due to increasing the heavy-to-light mass ratio m_2/m_1, we expect Δ_s/λ_{i+} to increase as a linear function of M, at least based on the binary weak shock formulation [14]. Examining post-shock terms in Eq. (25), the viscous term $\lambda_{\nu+}/\lambda_{i+} = (\rho c_s)_+/j$ is roughly constant (about 2) for the range of Mach numbers considered here ($M = 5$ to 11), and it in fact attains a maximum value of $\sqrt{5}$ for an infinite mass ratio or an infinite strength shock for a $\gamma = 5/3$ gas. In contrast, the ratios for species diffusion $\lambda_{D+}/\lambda_{i+}$ and thermal conductivity $\lambda_{\chi+}/\lambda_{i+}$ steadily increase with increasing mass ratio roughly as a linear function of $(m_2/m_1)^{1/2}$. For a fixed piston speed u_p, the Mach number also scales as $(m_2/m_1)^{1/2}$, hence Δ_s/λ_{i+} should vary as a linear function of Mach number. While this trend is observed in the continuum simulations, values of Δ_s/λ_{i+} in the MD simulations decrease for Mach numbers above 8. The kinetic and continuum analyses of shocks in plasmas in Refs. [58, 59] considered a single ion species with preheating by electron thermal conduction, so they are not particularly relevant to the simulations presented here with fixed electron temperature and binary mixtures. Nevertheless, they suggest that Δ_s/λ_{i+} approaches a constant as $M \to \infty$. `Miranda` simulations including electron preheating (cf. Fig. 5) with fixed piston speed $u_p = 80$ nm/ps show Δ_s/λ_{i+} increasing from 16 to 90 for mass ratios from $m_2/m_1 = 3$ to 20 ($M = 4.9$ to 10.7), while with fixed $m_2/m_1 = 3$ they show Δ/λ_{i+} increasing only from 16 to 19 for $u_p = 80$ to 180 nm/ps ($M = 4.9$ to 10.5), which is qualitatively consistent with these analyses. On the other hand, the PIC simulation results [2] for a shock in D-T plasma show a decline for Mach numbers greater than 6. The turnover in the scaled shock width observed in both PIC and MD simulations at high Mach numbers may be the result of highly nonlinear, nonequilibrium effects not captured in continuum models. Given the differences in species composition, thermodynamic conditions, and the treatment of electrons in these various studies, it's difficult to make a sensible quantitative comparison of actual ion shock widths, other than to note that they all exceed the ion mean free path by about an order of magnitude or more.

B. 1D multifluid continuum model

Based on the analysis of Ruyev, Fedorov, and Fomin [51], which neglects thermodiffusion terms, the steady shock equations for a binary mixture can be written

$$\partial\Big(\rho_\alpha v_\alpha v_\alpha + p_\alpha - (4\eta_\alpha/3)\partial v_\alpha\Big) = K_{\alpha\beta}(v_\beta - v_\alpha)\ , \quad (26)$$

$$\partial\Big(\rho_\alpha v_\alpha H_\alpha - (4\eta_\alpha/3)v_\alpha\partial v_\alpha - \kappa_\alpha\partial T_\alpha\Big) = c_{\alpha\beta}(T_\beta - T_\alpha) + K_{\alpha\beta}\hat{v}(v_\beta - v_\alpha)\ , \quad (27)$$

where $\beta \neq \alpha$ label different ionic species, v_α is the α-species velocity in the shock frame, and $\rho_\alpha v_\alpha = j y_{\alpha\pm} =$ constant; $H_\alpha = h_\alpha + v_\alpha^2/2$ where h_α is the enthalpy per unit mass, and $\hat{v} = (v_\alpha T_\beta/m_\beta + v_\beta T_\alpha/m_\alpha)/(T_\beta/m_\beta + T_\alpha/m_\alpha)$. Note that the more elaborate formulation by

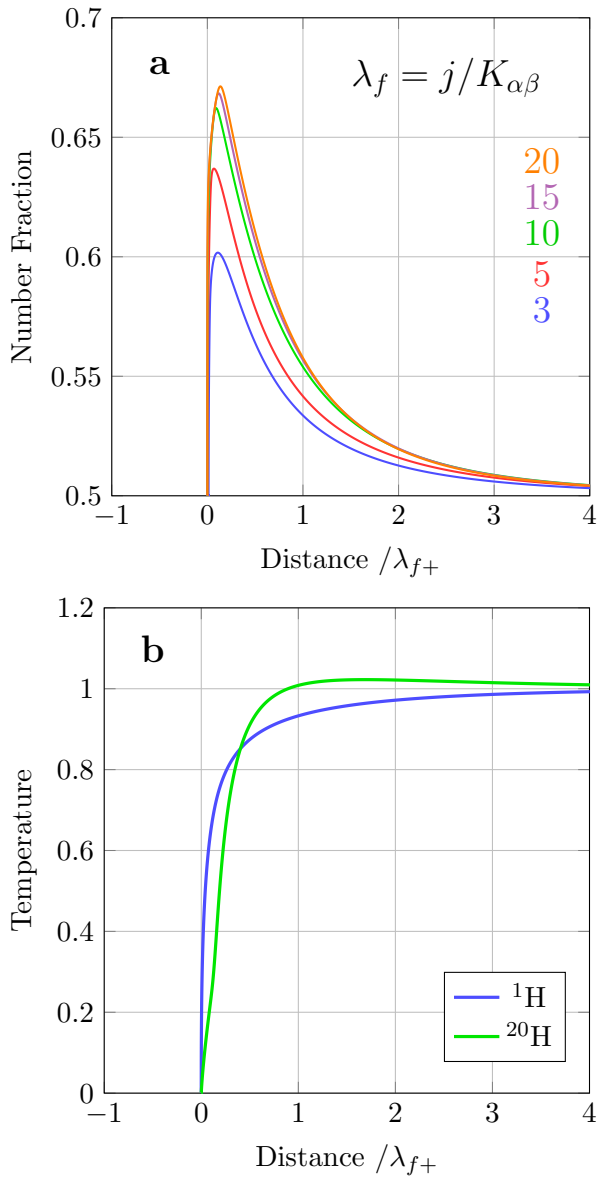

FIG. 10. The light-species number fractions in equimolar ^{1}H-^{n}H mixtures (**a**) and species temperature profiles for the ^{1}H-^{20}H mixture (**b**) from perfect-gas multifluid equilibrium solutions of the initial shock at the same Mach numbers in Table I plotted against the post-shock distance scaled by friction length.

Fernández de la Mora and Fernández-Feria [61] includes thermodiffusion terms and cross-transport terms for viscosity and conduction. To simplify the analysis further, a $\gamma = 5/3$ perfect gas is assumed, and the transport coefficients are approximated by $c_{\alpha\beta} = 3k_B K_{\alpha\beta}/(m_\alpha + m_\beta)$, $\eta_\alpha = (5\rho_\alpha p_\alpha/6)/(K_{\alpha\alpha} + K_{\alpha\beta})$, $\kappa_\alpha = 15k_B\eta_\alpha/4m_\alpha$, and $K_{\alpha\beta} \propto x_\alpha x_\beta/m_{\alpha\beta}(T_\beta/m_\beta + T_\alpha/m_\alpha)^{3/2}$. Pseudo-time-derivative terms are added to these equations to allow them to relax toward equilibrium, and solutions are shown in Fig. 10 with distance scaled by the friction length $\lambda_f = j/K_{\alpha\beta}$ evaluated behind the shock. The number density separation is not quite as large as in the single-fluid continuum simulations or the `ddcMD` simulations (cf. Table III), but follows the same trend; the temperature separation also resembles that seen in the `ddcMD` simulations (see Fig. 4), with a slight overshoot in the heavy-species temperature, ranging from about 1% to 2% over the far-field post-shock temperature for mass ratios of 3 to 20. There are very sharp shocks in the light species due to the abrupt drop in mean free path, as in the single-fluid continuum simulations, due to the neglect of kinetic effects. The width of the separation feature appears to scale as λ_{f+} for large mass ratios, and because $K_{\alpha\beta} = x_\alpha x_\beta p/D$ to 1st approximation in the CE model and $p \approx 3j^2/\rho$ behind a strong shock, this should scale asymptotically like λ_{D+}, similar to the single-fluid model.

VI. NON-MAXWELLIAN AND ANISOTROPIC EFFECTS IN MD

A. Anisotropic Temperatures

Molecular dynamics simulations allow us to calculate the anisotropic temperature components of each species at the shock. These distributions are shown in Fig. 11 for both species in an H-T mixture. In each simulated mixture, the increase of the longitudinal temperature component in the light species leads the increase of all other quantities. For both light and heavy species, the longitudinal temperature component has a sharp peak ahead of the shock. This spike is more pronounced in the heavy ions relative to the light ions, leading to the overshoot seen in the macroscopic temperature of the heavy species. Shock-normal temperatures remain higher than longitudinal temperatures for several nanometers, until longitudinal kinetic energy is redistributed through collisions. Thermal equilibrium is achieved in the heavy species at approximately the same point the mixture density reaches its post-shock value. This behavior is consistent with previous particle-based simulations of shocks in pure gasses [62, 63] and predictions of kinetics models [64, 65]. The source of this temperature spike can be found in the velocity distribution function (VDF) for each species near the shock.

B. Velocity Distribution Functions

Velocity functions (VDFs) and moments of the distribution are measured in 1 nm thick slabs parallel to the shock front. The average velocity is interpolated to each ion's position with a cubic polynomial when calculating the moments.

While the transverse VDF remains symmetric through the shock, the longitudinal VDF is skewed and non-Maxwellian in the shock front. The longitudinal VDFs of H and T at several locations across the shock are plotted in Fig. 12. The long tails associated with neg-

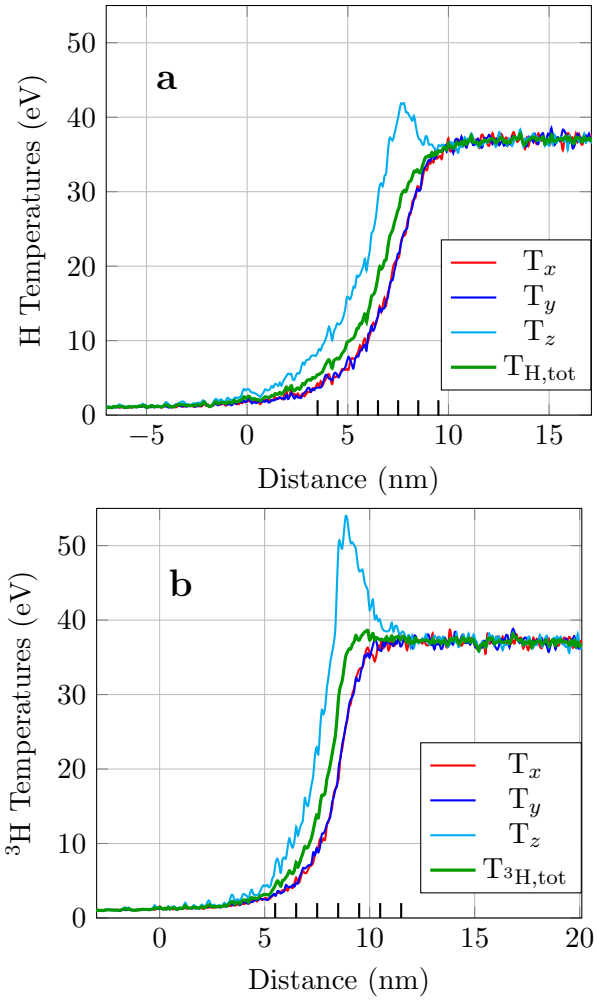

FIG. 11. Temperature components of H ions (**a**) and T ions (**b**) in the vicinity of the shock in an H-T mixture. Tick marks denote locations where the velocity distribution function is measured (see Fig. 12).

ative velocities in the VDFs far ahead of the shock can be attributed to fast ions that "leak out" from behind the shock. These hot ions carry enough energy across the shock to cause the initial rise in longitudinal temperature, creating the foot seen in temperature profiles of each species. However, these ions are not numerous enough to cause a noticeable rise in ion density.

VDFs become more skewed and less tail-heavy closer to the shock front. In this region, enough high-energy ions outrun the shock front to cause the density profiles to develop a foot that is not seen in continuum simulations. Velocity distributions return to a symmetric Maxwellian shape once thermalization completes, 2-3 nm behind the center of the shock front.

Because the continuum model assumes a single ion temperature for both species and Maxwellian velocity distributions, the nonthermal fast ions seen here are absent in continuum simulations. As a result, quantities such as density and temperature remain unaffected ahead of the continuum shock front.

The non-Maxwellian behavior in the transition region is in qualitative agreement with other kinetic shock calculations for plasmas [1, 2, 66] and neutral gasses [62, 67]. In particular, the velocity distribution functions found in Ref. [2] are strikingly similar to those in Fig. 12, despite Bellei *et al.* using an ion density that is four orders of magnitude lower than the mixtures investigated here.

Higher moments of the velocity distribution are shown in Fig. 13. The skewness of longitudinal VDFs is negative for both species, indicating that VDFs are generally skewed in the negative direction (ahead of the shock) in the transition region. For a fully developed shock in a hydrogen-tritium mixture, these moments begin to deviate from zero 20 nm ahead of the shock front for hydrogen and 10 nm ahead of the shock front for tritium. For each species, this jump coincides with the point where longitudinal temperature begins to increase and the increased skewness of the hydrogen VDF in the region $-20 \leq z \leq -10$ nm appears to have no effect on higher moments of the tritium velocity distribution in this region. Both the skewness and kurtosis of longitudinal velocities peak approximately 5 nm ahead of the temperature spike in each species seen in Fig. 11. Excess moments for both species return to zero at approximately the same point behind the shock. Skewness of transverse velocities remain close to zero across the shock while kurtosis of the transverse VDF peaks during the thermalization process. Transverse velocity kurtosis is positive, indicating a tail-heavy VDF during thermalization, with a magnitude less than the kurtosis for longitudinal velocities. The behavior of the moments for individual species in the mixture is qualitatively similar to the behavior seen in Ref. [62] for shocks in dense argon gas.

Interestingly, higher moments of these velocity distributions are affected far before any tail is visible in the VDFs shown in Fig. 12. This further indicates the presence of a small number of exceedingly fast ions in this region.

C. Strong Scattering Length and Collision Layer

The fast ions that skew velocity distributions far ahead of the shock must travel from the hot shocked region to their current position without thermalizing or losing an excessive amount of kinetic energy through collisions. As a result, we expect the fast ions in this layer ahead of the shock to have a high mean free path relative to ions in the surrounding plasma.

A profile of ion scattering length, as calculated by strong collisions in the MD simulations (see Section II B), is shown in Fig. 14. The figure also shows the local standard deviation of ion scattering length and the frequency of strong collisions in the region around the shock.

The strong collision scattering length is not noticeably different in pre-shock and post-shock regions, though at 0.13 nm it is about half the length of the macroscopic mean free path behind the shock, λ_{i+}, given in

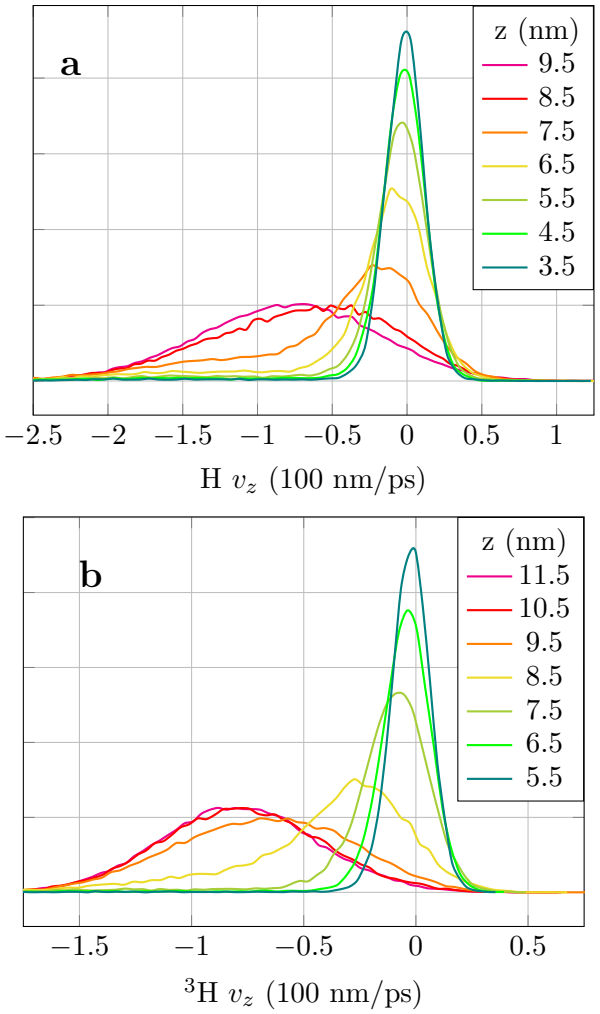

FIG. 12. Distributions of v_z in the light species (**a**) and heavy species (**b**) measured at several points throughout the H-T shock front. Labels refer to the z-coordinate at which the distribution was measured (see Fig. 11).

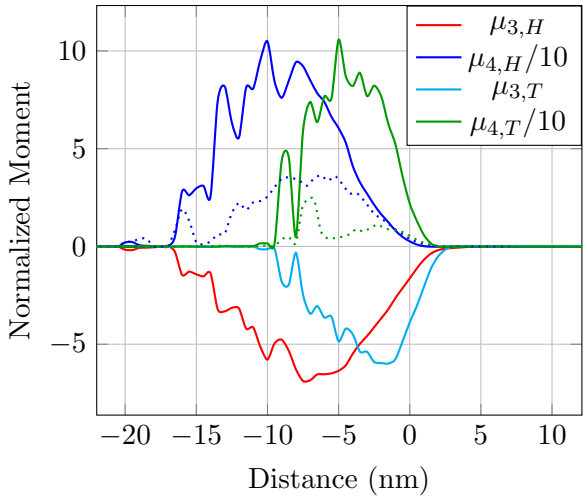

FIG. 13. Skewness (μ_3) and kurtosis (μ_4) of velocity distributions near the shock in a hydrogen-tritium mixture. Solid lines represent moments of longitudinal velocities while dotted lines are for transverse velocities. The shock front is located approximately at 0 nm. The skewness is essentially zero for the transverse velocities.

Table IV. The higher temperature and density behind the shock increases the frequency of strong collisions, but has a negligible impact on strong collision scattering length. Collision frequency is largest at the shock front, where slow material from ahead of the shock is accelerated to the post-shock bulk velocity. There is a 15-20 nm thick region ahead of the shock where collision frequency plateaus, but is still elevated relative to the pre-shock region. In this "collision layer," hot ions leaking out from behind the shock are accelerated by the electric field at the shock front and collide with cold ions ahead of the shock. The width and location of the collision layer in Fig. 14 show a strong correspondence to the non-Maxwellian regions in Fig. 13.

The scattering length of ions exhibits a small increase at the shock front/collision layer interface and reaches its maximum value at the leading edge of the collision layer. Spikes in the local variance of the scattering length are coincident with the spikes in scattering length.

The plateau of collision frequency and spike in strong collision scattering length further indicate that there is a collection of non-thermal fast ions that originate from strong collisions in the pre-shock layer and rush ahead into the colder unshocked plasma. These nonthermal ions travel through the colder material, leading to the non-Maxwellian distributions explored in Sections VI A and VI B. These ions also lead to a higher local scattering length and higher standard deviation of local scattering length, similar to their effect on velocities and higher moments of the velocity distribution ahead of the shock.

The collision frequency for ions in the pre-shock and post-shock regions can be estimated from the inverse of the slowing-down time for slow ions [68] using weak Chapman-Enskog collision rates

$$\omega \approx \sqrt{32}\frac{n_i k_B T_i}{\eta_{CE}} \tag{28}$$

and an impact parameter

$$\theta = \frac{(\overline{Z}e)^2}{k_B T_i}. \tag{29}$$

As seen in Table V, the collision frequency measured in MD simulations shows close correspondence with the prediction of the Chapman-Enskog model in the post-shock region. "Strong collision" molecular dynamics calculations are not tractable with the large impact parameter predicted by the CE model in the pre-shock region, so the post-shock impact parameter is used to calculate collision rates across the whole domain. Due to the smaller impact parameter used ahead of the shock, MD calculated collision frequencies fall well below the CE prediction.

TABLE V. Collision frequency ω and impact parameter θ predicted by the Chapman-Enskog model (CE) and calculated by molecular dynamics (MD) for an H-^{3}H mixture in the pre-shock (−) and post-shock (+) regions. Frequencies are in ps^{-1} and lengths are in nm. The MD collision length was assigned to be a small value during calculations and the CE collision length was found using Eq. (29).

model	ω_-	θ_-	ω_+	θ_+
CE	1310	0.770	1029	0.026
MD	20	0.026	1021	0.026

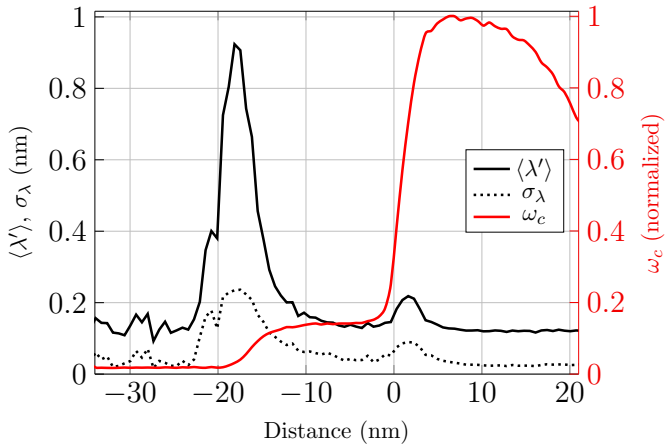

FIG. 14. Profiles of strong collision frequency (ω_c) and scattering length between strong collisions (λ') in an H-T mixture with impact parameter $\theta = 0.026$ nm. The standard deviation of particle scattering length (σ_λ) is denoted by a dotted line. Momentum mirrors are located at -40 nm and 22 nm and the shock front is near the 0 nm mark moving to the left.

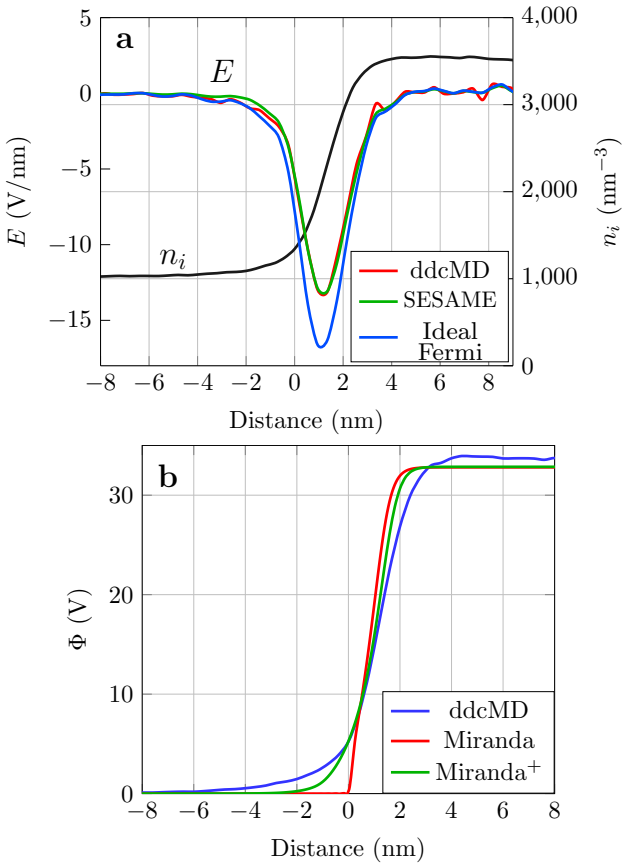

FIG. 15. The profile of the electric field (E) in an H-T mixture calculated by `ddcMD`, compared to the estimates of SESAME tables and calculations based on an ideal Fermi gas model in panel (**a**). Ion number density is shown to indicate shock location. The electric potential from `ddcMD` and from `Miranda`'s Ohm's law are shown in panel (**b**); "`Miranda+`" used the post-shock ion temperature in the ion transport coefficients to broaden the light ion shock.

D. Electric Field & Ion Reflection

A strong electric field is generated at the shock front by the high density inhomogeneity of the shock, which generally accelerates ions in the direction of the shock and prevents them from traversing from the preshock region into the postshock region. The electric potential in the MD simulations is computed from Coulomb's law from the electron density given by the multiscale orbital-free Thomas-Fermi calculation and the ion density. The electric field is the gradient of the total electric potential. The electric field is shown with mixture density in Fig. 15. At the shock front, the magnitude of the electric field reaches a maximum of 13 V/nm. The sign on the electric field is negative here, indicating that a positive ion will feel a force to the left (in the direction of shock motion).

The electric field predicted by the Chapman-Enskog model in the continuum code, which neglects magnetic fields and assumes charge neutrality between ions and electrons, is a general version of Ohm's law in the form

$$\mathbf{E} \approx \frac{\mathbf{j}_E}{\sigma_e} - \frac{n_e e}{\sigma_e}\sum_\alpha (z_\alpha - z_\alpha^{(2)})\frac{\mathbf{J}_\alpha}{\rho_\alpha} - S_e \nabla T_e - \frac{\nabla p_e}{n_e e}\ , \quad (30)$$

where $\mathbf{j}_E$ is the net electric current, σ_e is the electrical conductivity, z_α and $z_\alpha^{(2)}$ are ion charge and charge-squared fractions, $\mathbf{J}_\alpha$ is the species mass flux, and S_e is the thermoelectric coefficient; the second term on the right-hand side applies to mixtures with charge asymmetries, effectively modifying the electric current. Note the governing equations used in the continuum code are not directly affected by this "ambipolar" electric field; it is only used to eliminate interspecies Lorentz force terms in the diffusion model. For the present case of shocks in isotopic mixtures with no net electric current and no electron temperature gradient, Eq. (30) reduces simply to $\mathbf{E} \approx -(\nabla p_e)/n_e e$. This corresponds to a thermodynamic equilibrium between electric potential Φ and electron chemical potential μ_e such that $e\nabla\Phi \approx \nabla\mu_e = n_e^{-1}\nabla p_e$ (using the Gibbs-Duhem relation). Integrating the elec-

tric field measured in ddcMD across the shock gives an electric potential jump of about 34 V corresponding to an electron pressure jump of about 93 Mbar using this version of Ohm's law; the electric field profile is also in good agreement with Ohm's law when one associates the cold-curve pressure from the SESAME tables with the electrons, as seen in Fig. 15, except for some small differences at the leading edge of the shock on the left-hand side. The total electron pressure jump across the shock in the continuum code is 92 Mbar, corresponding to an electric potential jump of 33 V, which is in good agreement with the ddcMD results. Significant differences in shock width and structure, however, give rise to significantly different looking electric fields; because the H-T shock is somewhat narrower in the continuum code, peak values of about -20 V/nm are observed.

The Debye length for electrons is the scale on which charge separation can be appreciable; it has values of 0.03–0.04 nm in all cases, comparable to interatomic distances and the pre-shock ion mean free path, but much less than the post-shock ion mean free path and the overall width of the shock. Therefore any charge separation effects are expected to be extremely localized within the shocks. The electric field that is observed in this study of hydrogenic species is due in part to the spatially delocalized nature of the electron density relative to the ion density. Strictly speaking, the plasma remains locally charge neutral on the scale of the Debye length, however, the anisotropy in the density at the shock front gives rise to an electric field due to the density inhomogeneity in the plasma that is imposed by the shock. Our comparison of the Miranda and ddcMD electrostatic potential demonstrates that the major features of the electric field are captured by the gradient of the electron pressure in the continuum simulation.

Given the high electric field magnitude and large shock width visible in Fig. 15, it is clear that a majority of ions in the cold pre-shock region ($T_i = 1$ eV) lack the kinetic energy necessary to cross the shock front. In a collisionless plasma, this would lead to the reflection of ions at the shock front. As shown in Fig. 16, there is not a clearly visible group of reflected ions at the shock front, as was seen with shocks in 2D Yukawa systems [17]. The distribution of ion velocities shown here is qualitatively similar to the particle-in-cell (PIC) results presented by [2]. As in the PIC simulations, the high collision frequency at the shock front prevents the electric field from dominating the ion dynamics. Even using the strong collision scattering length as an analogue for ion mean free path (which is more likely to over-predict mean free path than underpredict it), the maximum ion mean free path is approximately 10% of the shock width. As a result, ions approaching the shock front undergo many collisions before they reach the turning point where they would be reflected by the electric field. This explains the scarcity of reflected ions at the shock front in Fig. 16 with speeds equal to twice the shock speed, despite the strong electric field in that region.

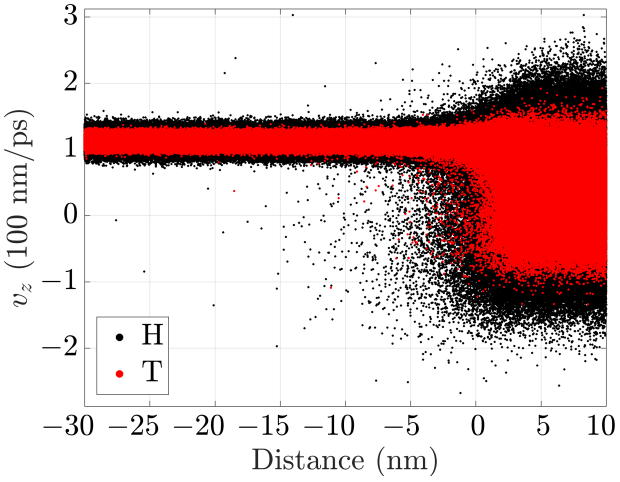

FIG. 16. A scatter plot of ion velocities at the shock front for an H-T mixture. Ion velocities have been shifted by $+v_s$ (112 nm/ps). Ions reflected by the shock front would appear clustered at $v_z = -112$ nm/ps.

VII. CONCLUSIONS

The propagation of strong shocks through binary plasma mixtures of hydrogen isotopes with disparate masses is simulated with molecular dynamics (using the ddcMD code) and continuum hydrodynamics (using the Miranda code). In molecular dynamics simulations, ions are simulated explicitly, with interactions specified by the Multiscale Orbital-free DFT Molecular Dynamics (MOD-MD) methodology. Continuum simulations use a single mass-weighted velocity, single ion temperature, and a standard Chapman-Enskog model to describe the transport of ion species. The KMD viscosity model is compared to MD results, finding that it works well for weakly to moderately coupled plasma mixtures at a temperature of 1 eV. Jump conditions and shock speeds computed with Miranda using the SESAME EOS are found to be in close agreement with MD results for mixtures with mass ratios between 3 and 20. This work demonstrates that, while the Miranda code is capable of describing general shock characteristics such as the jump conditions, shock speed, electric field, and species separation, certain kinetic effects are neglected at the shock front. In particular, anisotropic and non-Maxwellian velocity distributions are found at the shock front in the MD simulations. A spike in the longitudinal macroscopic temperature is seen for each species at their respective shock fronts. These spikes are caused by non-Maxwellian velocity distributions, the result of fast ions escaping from the hot region behind the shock. The presence of these fast ions is seen more clearly in measurements of collision frequency and scattering length in MD simulations. As measured by strong collisions, ion collision frequency is generally higher behind the shock than ahead of it; however a region of enhanced collision frequency is

found immediately in front of the shock. In this collision layer, fast ions from behind the shock front are stopped in the colder unshocked plasma. The scattering length of these non-thermal ions is found to be measurably longer than ions in the surrounding material. These ions deposit kinetic energy ahead of the shock front, leading to a foot in temperature and the non-Maxwellian velocity distributions at the shock front. With a collision length determined by the Chapman-Enskog model for the post-shock conditions, MD collision frequencies in the post-shock region show quantitative agreement with the CE model. As a result of the differences in the thermal properties ahead of the shock in the MD and continuum calculations, the detailed structure of the shock front differs between the two methods. We observe species separation in both calculations. The amount of spatial separation between the ion species is comparable, but the leading shock in the lighter species is unphysically sharp in the continuum simulations. This effect is largely the result of ion transport coefficients, which depend on the mean free path and are thus sensitive to the anisotopy in the temperature profile seen in the MD simulations. The transport coefficients drop by orders of magnitude across the shock because they are functions of local thermodynamic variables in the continuum model. The features of the post-shock density and temperature profiles are in better agreement than the pre-shock region due to thermalization of the plasma behind the shock front, which reestablilshes local thermodynamic equilibrium. These kinetic effects can lead to energy deposition in front of the shock, resulting in pre-heating of the unshocked material due to ion thermal conduction, increased shock width, and broadening of the separated region, especially for higher mass ratios.

Simulations of mixtures with larger mass ratios demonstrate an increased shock thickness. For the highest mass ratios simulated, distance between the shock in the light and heavy species is large enough for the mixture density to develop a "shoulder" structure. The maximum separation in species number fraction appears to asymptote at 0.21 in continuum simulations, while number fraction in MD simulations approaches the lower value of 0.18 with a broader and more symmetric separation feature.

The conditions explored here are generally colder than those relevant to ICF, and fully addressing the ICF-relevant conditions with MD requires the incorporation of electron thermal conduction and electron-ion coupling, which are planned as future developments of our MD capability. Nonetheless, the separation and kinetic effects explored here could influence isotope ratios in the hot spot during the implosion. At conditions typical for an ICF hot spot, the ion mean free path becomes large relative to characteristic grid size used in continuum simulations. When the mean free path is resolved in this manner, hydrodynamic simulations may over-predict shock "sharpness" by neglecting kinetic and separation effects caused by hot ions from behind the shock. This problem could be ameliorated to some extent with the use of non-local transport coefficients in continuum models or broadened diffusive fluxes in the continuum equations (e.g., [69]) that would allow the fluid to respond to the presence of the shock many mean free paths ahead of it; or the problem could be alleviated with the use of a hybrid scheme that resolves the shock front using particle-based methods and simulates the upstream and downstream material using a continuum hydrodynamic model, such as in Ref. [70].

Acknowledgments. This work was performed in part under the auspices of the U.S. Department of Energy by Lawrence Livermore National Laboratory under Contract DE-AC52-07NA27344. We gratefully acknowledge computer resources provided by Livermore Computing through a Computing Grand Challenge allocation. This work was funded in part by LLNL Laboratory Directed Research and Development 15-ERD-052. This material is based in part upon work supported by the Department of Energy, National Nuclear Security Administration, under Award Number DE-NA0002374. K. M. gratefully acknowledges support through the LLNL HEDP Summer Program. H. D. W. gratefully acknowledges support from the DOE PECASE award. LLNL-JRNL-733037

[1] C. Bellei, P. Amendt, S. Wilks, M. Haines, D. Casey, C. Li, R. Petrasso, and D. Welch, Phys. Plasmas **20**, 012701 (2013).
[2] C. Bellei, H. Rinderknecht, A. Zylstra, M. Rosenberg, H. Sio, C. Li, R. Petrasso, S. Wilks, and P. Amendt, Phys. Plasmas **21**, 056310 (2014).
[3] K. Molvig, N. M. Hoffman, B. J. Albright, E. M. Nelson, and R. B. Webster, Phys. Rev. Lett. **109**, 095001 (2012).
[4] B. J. Albright, K. Molvig, C.-K. Huang, A. N. Simakov, E. S. Dodd, N. M. Hoffman, G. Kagan, and P. F. Schmit, Phys. Plasmas **20**, 122705 (2013).
[5] M. Rosenberg, H. Rinderknecht, N. Hoffman, P. Amendt, S. Atzeni, A. Zylstra, C. Li, F. Séguin, H. Sio, M. G. Johnson, *et al.*, Phys. Rev. Lett. **112**, 185001 (2014).
[6] P. F. Schmit, K. Molvig, and C. W. Nakhleh, Phys. Plasmas **20**, 112705 (2013).
[7] B. I. Cohen, A. M. Dimits, G. B. Zimmerman, and S. C. Wilks, Phys. Plasmas **21**, 122701 (2014).
[8] S. Hsu, T. Joshi, P. Hakel, E. Vold, M. Schmitt, N. Hoffman, R. Rauenzahn, G. Kagan, X.-Z. Tang, R. Mancini, *et al.*, Europhys. Lett. **115**, 65001 (2016).
[9] L. Stanton, J. Glosli, and M. Murillo, preprint (2017).
[10] M. A. Gallis, T. P. Koehler, J. R. Torczynski, and S. J. Plimpton, Phys. Rev. Fluids **1**, 043403 (2016).
[11] A. W. Cook, W. H. Cabot, P. L. Williams, B. J. Miller, B. R. d. Supinski, R. K. Yates, and M. L. Welcome, in *Proceedings of the 2005 ACM/IEEE conference on Supercomputing* (ACM, 2005) p. 60.
[12] A. W. Cook, Phys. Fluids **19**, 055103 (2007).
[13] A. W. Cook, Phys. Fluids **21**, 055109 (2009).
[14] S. P. D'yakov, Zhur. Eksperim. Teor. Fiz **27**, 283 (1954).

[15] F. S. Sherman, J. Fluid Mech. **8**, 465 (1960).
[16] G. Bird, J. Fluid Mech. **30**, 479 (1967).
[17] M. Marciante and M. Murillo, Phys. Rev. Lett. **118**, 025001 (2017).
[18] J. Glosli, D. Richards, K. Caspersen, R. Rudd, J. Gunnels, and F. Streitz, in *Proceedings of the 2007 ACM/IEEE conference on Supercomputing* (ACM, 2007) p. 58.
[19] S. Kosuge, K. Aoki, and S. Takata, Eur. J. Mech. B-Fluid **20**, 87 (2001).
[20] T. Haxhimali, R. E. Rudd, W. H. Cabot, and F. R. Graziani, Phys. Rev. E **92**, 053110 (2015).
[21] F. R. Graziani, V. S. Batista, L. X. Benedict, J. I. Castor, H. Chen, S. N. Chen, C. A. Fichtl, J. N. Glosli, P. E. Grabowski, A. T. Graf, *et al.*, High Energ. Dens. Phys. **8**, 105 (2012).
[22] L. X. Benedict, M. P. Surh, J. I. Castor, S. A. Khairallah, H. D. Whitley, D. F. Richards, J. N. Glosli, M. S. Murillo, C. R. Scullard, P. E. Grabowski, *et al.*, Phys. Rev. E **86**, 046406 (2012).
[23] P. E. Grabowski, M. P. Surh, D. F. Richards, F. R. Graziani, and M. S. Murillo, Phys. Rev. Lett. **111**, 215002 (2013).
[24] H. D. Whitley, C. R. Scullard, L. X. Benedict, J. I. Castor, A. Randles, J. N. Glosli, D. F. Richards, M. P. Desjarlais, and F. R. Graziani, Contrib. Plasma Phys. **55**, 192 (2015).
[25] M. P. Desjarlais, C. R. Scullard, L. X. Benedict, H. D. Whitley, and R. Redmer, Phys. Rev. E **95**, 033203 (2017).
[26] S. Hau-Riege and J. Weisheit, Phys. Rev. E **91**, 033106 (2015).
[27] S. P. Hau-Riege and J. Weisheit, Phys. Rev. E **95**, 013204 (2017).
[28] T. Haxhimali and R. E. Rudd, in *Frontiers and Challenges in Warm Dense Matter* (Springer, 2014) pp. 235–263.
[29] T. Haxhimali, R. E. Rudd, W. H. Cabot, and F. R. Graziani, Phys. Rev. E **90**, 023104 (2014).
[30] D. F. Richards, J. N. Glosli, B. Chan, M. R. Dorr, E. W. Draeger, J.-L. Fattebert, W. D. Krauss, T. Spelce, F. H. Streitz, M. P. Surh, and J. A. Gunnels, in *Proceedings of the Conference on High Performance Computing Networking, Storage and Analysis*, SC '09 (ACM, New York, NY, USA, 2009) pp. 60:1–60:12.
[31] For information on the Vulcan supercomputer see https://hpc.llnl.gov/hardware/platforms/vulcan.
[32] A. Randles, E. W. Draeger, T. Oppelstrup, L. Krauss, and J. A. Gunnels, in *Proceedings of the International Conference for High Performance Computing, Networking, Storage and Analysis* (ACM, 2015) p. 1.
[33] R. Courant and D. Hilbert, *Methods of Mathematical Physics*, Vol. 1 (Interscience, New York, 1953).
[34] Y. B. Zeldovich and Y. P. Raizer, *Physics of Shock Waves and High Temperature Hydrodynamic Phenomena* (Academic Press, New York, 1966).
[35] H. Brysk, Plasma Physics **16**, 927 (1974).
[36] Y. T. Lee and R. M. More, The Physics of Fluids **27**, 1273 (1984).
[37] S. I. Braginskii, in *Reviews of Plasma Physics*, edited by M. A. Leontovich (Consultants Bureau, New York, 1965) pp. 205–311.
[38] E. M. Epperlein and M. G. Haines, The Physics of Fluids **29**, 1029 (1986).
[39] G. Bird, J. Fluid Mech. **31**, 657 (1968).
[40] K. Whitney, Phys. Plasmas **6**, 816 (1999).
[41] K. Molvig, A. N. Simakov, and E. L. Vold, Phys. Plasmas **21**, 092709 (2014).
[42] S. Chapman and T. G. Cowling, *The Mathematical Theory of Non-Uniform Gases* (Cambridge University Press, London, 1970).
[43] J. M. Burgers, *Flow Equations for Composite Gases* (Academic Press, New York, 1969).
[44] C. Paquette, C. Pelletier, G. Fontaine, and G. Michaud, Astrophys. J. Suppl. Ser. **61**, 177 (1986).
[45] L. G. Stanton and M. S. Murillo, Physical Review E **93**, 043203 (2016).
[46] M. S. Murillo, High Energ. Dens. Phys. **4**, 49 (2008).
[47] J. D. Ramshaw and A. W. Cook, Phys. Plasmas **21**, 022706 (2014).
[48] S. P. Lyon and J. D. Johnson, Los Alamos National Laboratory, Los Alamos, NM, LA-UR-92-3407 (1992).
[49] R. M. More, *Handbook of Plasma Physics*, Vol. 3 (Elsevier, Amsterdam, 1991).
[50] L. Landau and E. Lifshitz, *Fluid Mechanics, Landau and Lifshitz, Course of Theoretical Physics*, 2nd ed., Vol. 6 (Butterworth-Heinemann, Oxford, 1987).
[51] G. Ruyev, A. Fedorov, and V. Fomin, J. Appl. Mech. Tech. Phys. **43**, 529 (2002).
[52] B. L. Holian, W. G. Hoover, B. Moran, and G. K. Straub, Phys. Rev. A **22**, 2798 (1980).
[53] E. Salomons and M. Mareschal, Phys. Rev. Lett. **69**, 269 (1992).
[54] Y. G. Ohr, Phys. Fluids **13**, 2105 (2001).
[55] J.-P. Hansen and I. R. McDonald, *Theory of simple liquids* (Elsevier, 1990).
[56] R. E. Rudd, W. H. Cabot, K. J. Caspersen, J. A. Greenough, D. F. Richards, F. H. Streitz, and P. L. Miller, Phys. Rev. E **85**, 031202 (2012).
[57] E. Goldman and L. Sirovich, J. Fluid Mech. **35**, 575 (1969).
[58] M. Y. Jaffrin and R. F. Probstein, The Physics of Fluids **7**, 1658 (1964).
[59] M. S. Greywall, The Physics of Fluids **18**, 1439 (1975).
[60] H. Salwen, C. E. Grosch, and S. Ziering, The Physics of Fluids **7**, 180 (1964).
[61] J. Fernandez de la Mora and R. Fernandez-Feria, Phys. Fluids **30**, 2063 (1987).
[62] S. Schlamp and B. C. Hathorn, J. Comput. Phys. **223**, 305 (2007).
[63] O. Kum, W. G. Hoover, and C. Hoover, Phys. Rev. E **56**, 462 (1997).
[64] L. H. Holway Jr, Phys. Fluids **8**, 1905 (1965).
[65] S.-M. Yen, Phys. Fluids **9**, 1417 (1966).
[66] F. Vidal, J. Matte, M. Casanova, and O. Larroche, Phys. Fluids B **5**, 3182 (1993).
[67] P. Valentini and T. E. Schwartzentruber, Phys. Fluids **21**, 066101 (2009).
[68] N. Krall and A. Trivelpiece, *Principles of Plasma Physics* (McGraw-Hill, New York, 1973).
[69] G. Schurtz, P. Nicolaï, and M. Busquet, Phys. Plasmas **7**, 4238 (2000).
[70] T. E. Schwartzentruber and I. D. Boyd, J. Comput. Phys. **215**, 402 (2006).